2015

Development and application of numerical models for simulating bio-oil gasification

Arian Jafari
Iowa State University

Development and application of numerical models for simulating bio-oil gasification

by

Arian Jafari

A thesis submitted to the graduate faculty

in partial fulfillment of the requirements for the degree of

MASTER OF SCIENCE

Major: Mechanical Engineering

Program of Study Committee:
Song-Charng Kong, Major Professor
Alberto Passalacqua
Jonathan D. Regele

Iowa State University

Ames, Iowa

2015

TABLE OF CONTENTS

LIST OF FIGURES

LIST OF TABLES

ACKNOWLEDGEMENTS

This project would not have been possible without the support of many people. First and foremost I would like to express my sincere gratitude to my advisor, Dr. Song-Charng Kong, for his excellent guidance, caring, patience, and providing me with an excellent atmosphere for doing research. Besides my advisor, I would like to thank the rest of my committee members, Dr. Alberto Passalacqua and Dr. Jonathan Regele for being in my committee. I would like to acknowledge the financial support of Iowa Energy Center.

I would like to thank my fellow labmates in Dr. Kong's research group, particularly, Dr. Sujith Sukumaran, and Cuong Van Huynh for their help throughout my study at Iowa State University.

My deepest gratitude goes to my family for their endless love and support throughout my life. It was under their watchful eyes that I gained so much drive and an ability to tackle challenges.

ABSTRACT

Bio-oil, a mixture of complex oxygenated hydrocarbons, is obtained through fast pyrolysis of solid biomass. As biomass is low in energy density and not easily transportable, a novel approach is to convert biomass to bio-oil, transport bio-oil to a centralized facility, gasify bio-oil to syngas, and upgrade syngas to transportation fuels and other high-value chemicals. In this study, a comprehensive numerical model was developed to simulate the gasification of bio-oil at different operating conditions and different reactor geometries.

The present model considers spray, atomization, vaporization, and chemical reactions of bio-oil. Bio-oil was modeled as a multi-component fuel, consisting of ten major components. The Joback method, a group contribution method, was used to calculate the bio-oil thermophysical properties, including enthalpy, latent heat, and vapor pressure. With the bio-oil thermophysical properties, vaporization of single bio-oil drop was simulated, and results show that the heaviest component, i.e., levoglucosan, is the last component which remains in the drop.

A thermodynamic equilibrium approach was used to account for chemical reactions. Gasification of methanol was first simulated for model validation. The numerical simulations of bio-oil gasification at different operating pressures and equivalence ratios were also conducted. Comparisons between the numerical results and experimental data show that the current model can predict gasification process reasonably well. Results show that syngas yield is independent of the ambient pressure while sensible to equivalence ratio. The simulation results show that conversion of bio-oil to syngas occurs gradually along the gasifier.

Using the current model, bio-oil gasification was studied for large reactors with high gasification capacity. It was found that a reactor with 30 cm in diameter and 300 cm in length can

gasify bio-oil at a rate of 6 ton/day and the gasification products can reach their equilibrium state at the reactor outlet. It is estimated that a gasifier with 200 cm in diameter and 300 cm in length can allow the use of 20 injectors to gasify 120 ton/day of bio-oil. Therefore, it is suggested that 10 such gasifiers can be assembled in a biorefinery to achieve the capacity of 1200 tons of bio-oil per day. This quantity of bio-oil corresponds approximately to 2000 ton/day of solid biomass that is used for fast pyrolysis to produce 1200 ton/day of bio-oil.

CHAPTER 1. INTRODUCTION

1.1 Motivation

Basically the energy stored in biomass is the solar energy that biomass has received during its growth. Man can use this energy by direct combustion to produce heat or conversion to various forms of biofuels. Unlike fossil fuels which take millions of years to form, plants as a main source of biomass use sunlight through photosynthesis, absorb atmospheric carbon dioxide, and metabolize it to grow. When biomass burns, it releases the carbon dioxide which it has absorbed from atmosphere over the past years, months or days; overall it does not augment the Earth's carbon dioxide inventory.

Biomass energy is abundant and can be utilized in various ways. Economically, biomass can help improve the energy security, enhance the productivity of agriculture, and mitigate the waste. Among all of the renewable energy sources, biomass is considered a promising renewable alternative to fossil fuels and its utilization has grown rapidly.

Biomass is available over a wide range of regions, however, it may not be very reliable because of its dependency on the season, relatively low energy density, and high transportation cost. In light of the aforementioned problems, researchers have been working on two main pathways in converting biomass to valuable products, namely biochemical and thermochemical pathways. While biochemical conversion of biomass uses enzymes, bacteria, and microorganisms to break down biomass into gaseous or liquid fuels, thermochemical conversion involves the use of heat at relatively high temperatures to decompose biomass into energy products through pyrolysis and gasification processes.

Bio-oil, a mixture of complex oxygenated hydrocarbons, is obtained through the fast pyrolysis of solid biomass. As biomass is low in energy density and not easily transportable, a novel approach is to convert biomass to bio-oil, transport bio-oil to a centralized facility, gasify bio-oil to syngas, and upgrade syngas to transportation fuels and other high-value chemicals. Some experimental studies have been done on bio-oil gasification but no numerical modeling of bio-oil gasification has been performed so far.

1.2 Objective

The objective of this study is to numerically investigate the gasification of bio-oil and develop a computational tool to characterize reactor performance. The present numerical model will simulate bio-oil spray atomization, vaporization, mixing, and chemical reactions inside a gasifier. The numerical results will be compared with experimental data of syngas composition. The numerical model will be used to determine the proper design parameters, including reactor size, fuel injection rate, and operating conditions.

CHAPTER 2. BACKGROUND AND LITERATURE REVIEW

2.1 Pyrolysis

Pyrolysis is thermochemical decomposition of organic materials at high temperatures (between 300 to 650 ℃) in the absence of oxygen into a range of useful products [1]. In practice, it is not possible to achieve a completely oxygen-free process due to the presence of small amount of oxygen in the system, causing a minor oxidation. During pyrolysis, complex biomass molecules break down into various molecules of gas, liquid, and char. Heat transfer rate and the type of biomass are two factors that can influence bio-oil yields during the pyrolysis process. Based on heat transfer rate and the type of the medium, pyrolysis can be categorized into slow, fast and hydropyrolysis. Slow pyrolysis is mostly used in char production by gradually heating the biomass in an oxygen-deprived medium, resulting in the highest carbon sequestration potential. Unlike early pyrolyzers (slow pyrolysis) which were designed to maximize the char production, modern pyrolyzers are mainly designed to produce gas and liquid yields. In fast pyrolysis, biomass is heated up to peak temperature so rapidly before it decomposes. The peak temperature should be kept below 650 ℃ for bio-oil production but for gas production it can be high up to 1000 ℃. Flash pyrolysis and ultra-rapid pyrolysis are two types of fast pyrolysis in which the temperature is around 450 to 600 ℃ and 1000 ℃, respectively.

Chemical industries have taken the advantage of pyrolysis for the production of methanol [2], charcoal, syngas [3-6], bio-oil, and etc. Figure 2.1 illustrates the process in a typical biomass facility of fast pyrolysis to produce bio-oil.

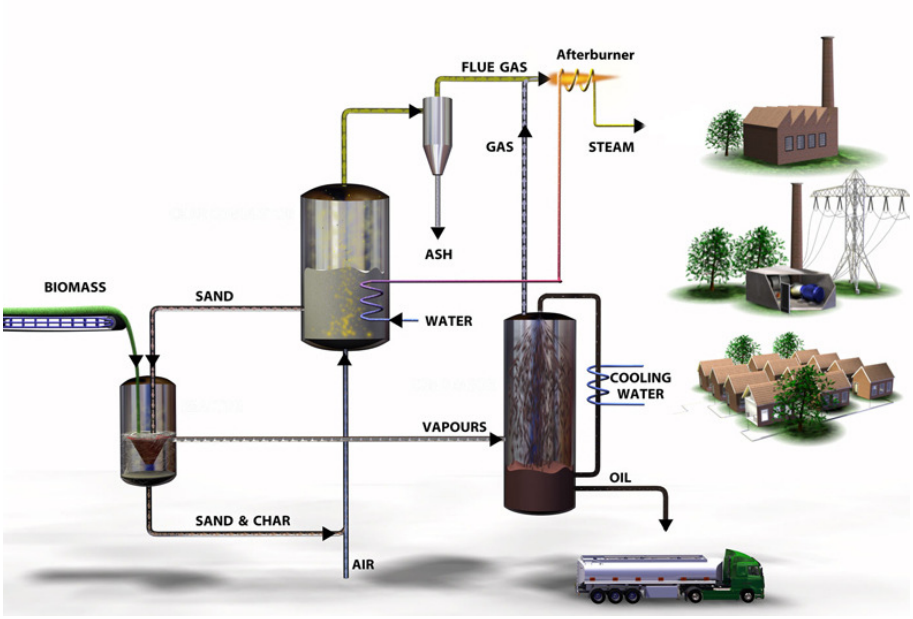

Figure 2.1. Schematic of biomass fast pyrolysis to produce bio-oil

Biomass is fed into a pyrolysis chamber where it meets the hot solids (fluidized bed), heating the biomass to the pyrolysis temperature, to start the thermal decomposition. The condensable and no condensable vapors released from the biomass leave the chamber, while the resulting char are directed to another chamber where high pressure air is used to retrieve the sand. The gas is separated from the char and cooled at downstream of the reactor. The condensable vapor condenses as bio-oil, or pyrolysis oil. The overall chemical reaction through the pyrolysis process can be presented as [1]

$$C_n H_m O_p \,(Biomass) \xrightarrow{Heat} \sum_{liquid} C_x H_y O_z + \sum_{gas} C_a H_b O_c + H_2O + C\,(char) \qquad (2.1)$$

As stated earlier, biomass pyrolysis converts the complex biomass molecules into gas, liquid, and solid. The liquid, known as bio-oil, can be upgraded to other hydrocarbon fuels or turned into syngas and other high-value chemicals through gasification process. Fast pyrolysis is more common in production of bio-oil and gas while slow pyrolysis is mostly used in char production. Studies has shown that a rapid thermal decomposition in the absence of oxidizer results

in production of char, bio-oil (up to 80%) [7], and tar. Numerous chemical mechanisms take place during biomass pyrolysis, and based on each mechanism different type of products will be obtained. The most well-known mechanisms in pyrolysis process can be classified as those which result in production of anhydro-sugars through secondary cracking, 5-hydroxymethyl-furfural (5-HMF) and furfural (FF), hydroxyacetaldehyde, and levoglucosan. For example, pyrolysis of pure cellulose with pretreatment with dilute acid yields to production of levoglucosan up to 50%. Shafizadeh et al. [8] reported that methanol, acetic acid, and char are possible by-products of this process. They also showed that pretreatment of cellulose including prehydrolysis with dilute acid can increase the levoglucosan production from 57% to 78%.

Table 2.1 shows different types of biomass, reactors, pyrolysis, and operating conditions being used in bio-oil production. The pyrolysis yield depends on biomass composition including its hydrogen to carbon ratio (H/C), size, shape, and structure. It also depends on the pyrolysis temperature [9-11], heat transfer rate [12, 13], and residence time [14-17] in the reaction zone. Each of the biomass major compositions has its own physical and chemical properties which can affect the pyrolysis product. For instance, hemicellulose is the main source of volatile products and the temperature range for its decomposition lies between 150 to 350 ºC. On the other hand, lignin decomposes over a broader range of temperature and produces more aromatic and char.

Table 2.1. Different types of biomass and their corresponding processes in bio-oil production

Biomass type	Type of reactor	Temp. (°C)	Bio-oil yield (wt%)	Types of pyrolysis
Grape bagasse	Stainless steel fixed-bed reactor [18]	550	27.6	Fast pyrolysis
Hardwood & softwood from pine tree	Tubular vacuum pyrolysis reactor [19]	450	55.0	Fast pyrolysis
Municipal, livestock and wood waste	Internal circulating fluidized-bed (ICFB) reactor [20]	500	39.7	Fast pyrolysis
Plant thistle, Onopordum acanthium	Fixed-bed reactor [21]	550	27.3	Slow pyrolysis
Potato skin	Stainless steel fixed-bed reactor [22]	550	24.8	Steam pyrolysis
Pinewood sawdust	Conical spouted bed reactor [23]	500	75.0	Flash pyrolysis
Pine wood	Auger reactor [24]	450	50.0	Fast pyrolysis
Waste furniture sawdust	Fluidized-bed reactor [25]	450	65.0	Fast pyrolysis
Rice husks	Fluidized-bed reactor [26]	450	60.0	Fast pyrolysis
Sugar cane waste	Fixed-bed fire-tube heating reactor [27]	475	56.0	Fast pyrolysis
Corn cobs & corn stover	Bubbling fluidized bed reactor [28]	650	61.6	Fast pyrolysis
Laurel (Laurus nobilisL.) extraction	Fixed-bed reactor [29]	500	21.9	Fast pyrolysis
Corncob	Fluidized-bed reactor [30]	550	56.8	Fast pyrolysis
Jute stick	Continuous feeding fluidized bed reactor [31]	500	66.7	Fast pyrolysis
Apricot pulp	Fixed-bed reactor [32]	550	22.4	Fast pyrolysis
Wood sawdust	Cyclone reactor [33]	650	74.0	Fast pyrolysis

In the early days of biomass pyrolysis, it was thought that particle size of a few hundred microns was needed for complete reaction. Smaller particles (approximately 2 mm in size [36]) can allow fast heat transfer to produce condensable gas and yield more bio-oil production. Demirbas [37] studied the effect of temperature on pyrolysis product and found that at low temperatures more char would be produced whilst lower char yield is obtained at high temperatures. The yield of liquid products from biomass fast pyrolysis increases with temperature

up to 500-700 K and after that experiences a reduction as temperature increases further up to 1200 K. Based on what product is of primary interest, the optimum temperature of biomass pyrolysis can be selected. It must be noted that different types of biomass have different behaviors toward the temperature change and it should be considered in design procedure. In addition to temperature, heating rate also plays an important role especially when it comes to bio-oil production. In order to obtain the maximum yield of bi-oil, high heat transfer rate accompanied with a moderate final temperature (450-600 ºC) and short gas residence time is recommended [1]. Biomass pretreatment, such as hydrolysis with acid/base at 25 ºC to 122 ºC at atmospheric pressure, was reported by Cunha et al. who obtained high quality bio-oil [38]. Further investigations of reducing the oxygen content of biomass by using the acid or base were studied by Das et al. [39] and Kumar et al. [40].

Bio-oil, also known as bio-fuel oil, pyrolysis oil or liquid wood [41, 42], can be transported to chemical facilities for converting into syngas or other high-value chemicals. Bio-oil is rather high viscous, dark brown in color and composed of many different types of hydrocarbons up to 300 different components [32, 43]. Water, phenol derivatives, sugars, alcohols, phenols, esters, amines and lignin derived substances can be found in bio-oil [32].

Being a highly complex composition, bio-oil is difficult to analyze and characterized [44], and especially for numerical simulation some simplified assumption should be done [45]. Using the gas chromatography-mass spectrometry (GC-MS) [46], the major components of an example of bio-oil are listed in Table 2.2 [47]. As mentioned earlier, the most popular process in producing bio-oil from biomass is fast pyrolysis [18-35].

Table 2.2. Components of crude bio-oil [47]

Main components	RT/min	Area w/%
3-methyl-5H-furan-2-one	5.19	0.38
corylon	6.15	1.18
phenol	6.59	1.57
o-cresol	6.8	1.12
m-cresol	7	1.46
2-methoxy-6-methyl-phenol	7.79	1.78
3,4-dimethyl-phenol	8.99	1.14
4-ethyl-phenol	9.7	1.31
3-(2-hydroxy-phenyl)-acrylic acid	10.1	1.53
catechol	10.81	3.53
3-methyl-catechol	11.9	1.36
vanillin	12.7	0.24
4-ethyl-catechol	12.86	0.71
levoglucosan	14.73	9.95
3-(4-hydroxy-2-methoxy-phenyl)-propenal	15.8	0.15
formaldehyde	1.42	3.14
aldehyde	1.51	6.52
hydroxyacetaldehyde	1.61	3.14
hydroxypropanone	1.72	2.70
butyric acid	1.82	0.96
acetic acid	2.07	29.76
glyceraldehyde	2.6	3.54
3,4-dihydroxy-dihydro-furan-2-one	2.77	3.27
2,2-dimethoxy-ethanol	2.86	6.83
furfural	3.13	6.56
2,5-dimethoxy-tetrahydro-furan	3.5	3.47
4-hydroxy-butyric acid	4.27	0.43
5H-furan-2-one	4.51	0.74
2,3-dimethyl-cyclohexanol	4.76	1.31
2,3,4-trimethoxy-benzaldehyde	1.42	3.14

During the past few decades, bio-oil and its derivatives have been recognized as a possible substitute for petroleum-based fuels. However, researchers mainly focus on production of bio-oil, and improving its physical and chemical characteristics, few attempts have been done to study the spray, vaporization, and its chemical kinetics [45, 48-50]. A detailed review of spray and vaporization will be provided in further sections.

2.2 Gasification

The history of gasification dates back to seventeenth century where Thomas Shirley in 1669 conducted a set of experiments with carbureted hydrogen. Thirty years later after a couple of well-designed pyrolitic experiments, Dean Clayton succeeded in obtaining coal gas (1699). Many years after William Murdoch for the first time used coal gas to lighten up a room in his house, coal was one the essential fuels used for lightening purposes in England due to its lower cost compared to oil lamps or candles (about 75% less) [53]. During 1850-1940, the need for lighting (either streets or home and factories) and heating was supplied by the gas made from coal. During World War II German engineers decided to rely on gasification to produce synthetic gas due to Allied bombardment on their oil refineries. During this period over a million gasifiers in different shapes and sizes were built to meet the growing transportation demand.

In the 1950s the gasification technology was exported to South Africa where it experienced further development in producing liquid fuels and chemicals (e.g., fertilizers). During 1975-1990, U.S. government appropriated a great funding for economically acceptable gasification projects which led to the concept of the Integrated Gasification Combined Cycle (IGCC) power plant. The current period of gasification evolution has inaugurated due to concerns related to global warming, the need for a reliable and easy-to-access energy source, and avoiding unpredicted political crisis

(which has a direct effect on fossil fuels price). As a result, IGCC facilities has attracted interests from commercial developers.

As mentioned earlier, bio-oil has numerous advantages over biomass, such as its high heating value, and its easily transportable and storing characteristics [54-52]. It can also be added to petroleum-based fuels improving the combustion efficiency [45]. Similar to biomass pyrolysis, the gasification of bio-oil also results in production of syngas and other simple and light hydrocarbons. The main difference between gasification and pyrolysis can be attributed to their reaction temperature and the oxygen level. Unlike pyrolysis which takes place at temperature range between 400 ℃ and 700 ℃ in the absence of oxygen, gasification process needs a higher temperature range of 800 ℃ to 1800 ℃ with 25% theoretical oxygen, depending on the characteristic of the feedstock [1]. Due to high reaction temperature most of the gasification modeling are based on the thermodynamic equilibrium [1].

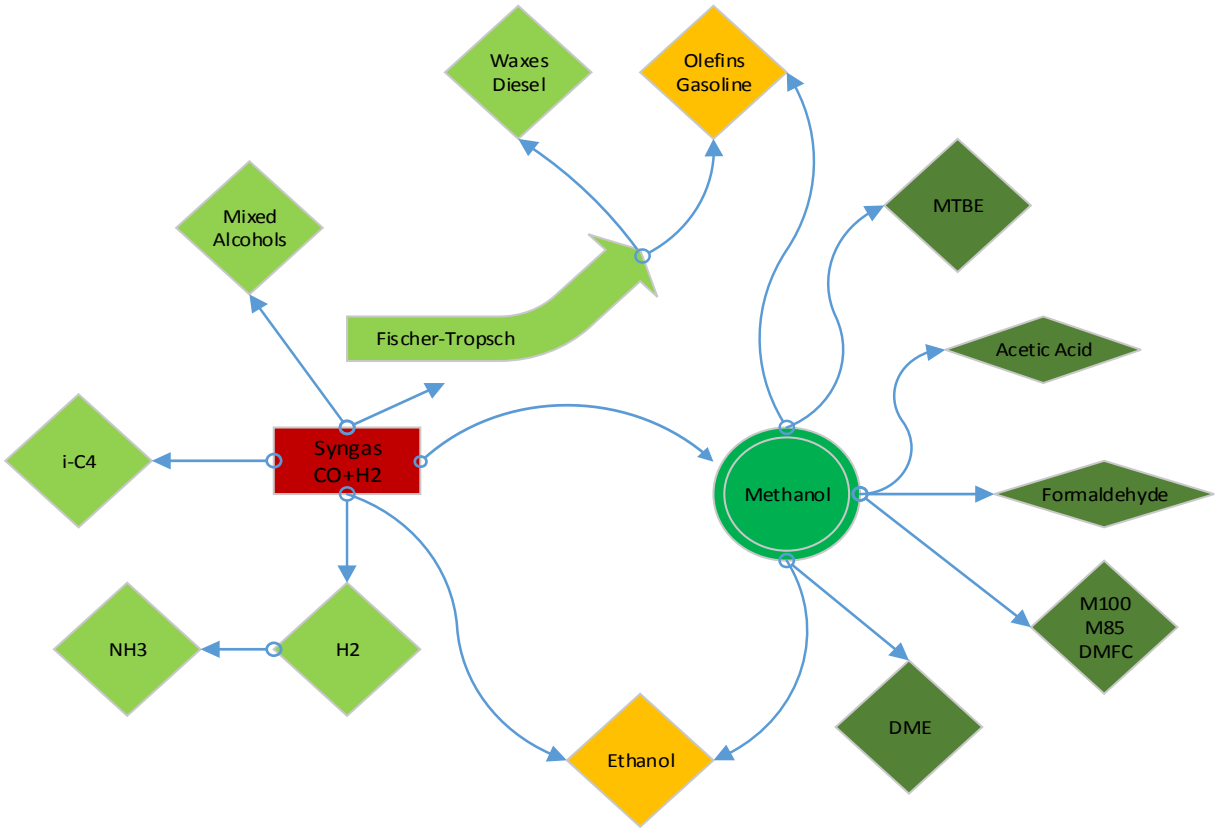

Figure 2.2. Diagram of syngas conversion processes

Syngas, as the main product of gasification, is a highly valued gas mixture which can be processed further in chemical industries to produce liquid fuels and high-value chemicals. Figure 2.2 shows the different paths which syngas goes through producing new products.

The overall gasification reaction can be written as

$$C_n H_m + \frac{n}{2} O_2 = nCO + \frac{m}{2} H_2 \qquad (2.2)$$

where for gas, as pure methane, m=4 and n=1, hence m/n=4; for oil, m/n ≈ 2, hence m=2 and n=1; for coal, m/n ≈ 1, hence m=1 and n=1.

For example, gasification of solid carbon includes many chain reactions [55] listed through Eq.(2.3) to (2.16) .At the beginning, CO_2 reacts with a free site of carbon C_{fas} producing carbon monoxide and a carbon-oxygen surface complex, C(O) [56]. Then carbon-oxygen surface complex produces more carbon monoxide. The most important reaction through gasification process can be attributed to dissociation of water on a free active site of carbon which results in production of hydrogen and carbon-oxygen surface complex. This C(O) produces further carbon monoxide. Shift reaction is also important during the gasification process and can enhance the production of hydrogen in the cost of reducing carbon monoxide. Person and Werther [57] reported that pressure has no significant effect on this reaction while the reaction can move in favor of either hydrogen or carbon monoxide production at different temperatures. As gasification is an endothermic process, partial exothermic reactions, including $C+\frac{1}{2}O_2 \rightarrow CO$ and $C+O_2 \rightarrow CO_2$ are allowed to shoulder the heat supply.

Boudouard reaction	$C+CO_2 \leftrightarrow 2CO+172\,kJ.mol^{-1}$	(2.3)
Water-gas or steam	$C+H_2O \leftrightarrow CO+H_2+131\,kJ.mol^{-2}$	(2.4)
hydrogasification	$C+2H_2 \leftrightarrow CH_4-74.8\,kJ.mol^{-2}$	(2.5)
Combustion reaction	$C+\frac{1}{2}O_2 \rightarrow CO-111\,kJ.mol^{-1}$	(2.6)
Oxidation reaction #1	$C+O_2 \rightarrow CO_2-394\,kJ.mol^{-2}$	(2.7)
Oxidation reaction #2	$CO+\frac{1}{2}O_2 \rightarrow CO_2-284\,kJ.mol^{-4}$	(2.8)
Oxidation reaction #3	$CH_4+2O_2 \leftrightarrow CO_2+2H_2O-803\,kJ.mol^{-3}$	(2.9)

Oxidation reaction #4 $$H_2 + \frac{1}{2}O_2 \rightarrow H_2O - 242\,kJ.mol^{-4} \quad (2.10)$$

Water-gas shift reaction $$CO + H_2O \leftrightarrow CO_2 + H_2 - 41.2\,kJ.mol^{-4} \quad (2.11)$$

Methanation reaction #1 $$2CO + 2H_2 \rightarrow CH_4 + CO_2 - 247\,kJ.mol^{-4} \quad (2.12)$$

Methanation reaction #2 $$CO + 3H_2 \leftrightarrow CH_4 + H_2O - 206\,kJ.mol^{-4} \quad (2.13)$$

Methanation reaction #3 $$CO_2 + 4H_2 \rightarrow CH_4 + 2H_2O - 165\,kJ.mol^{-2} \quad (2.14)$$

Steam-reforming reaction #1 $$CH_4 + H_2O \leftrightarrow CO + 3H_2 + 206\,kJ.mol^{-3} \quad (2.15)$$

Steam-reforming reaction #2 $$CH_4 + \frac{1}{2}O_2 \rightarrow CO + 2H_2 - 36\,kJ.mol^{-3} \quad (2.16)$$

2.3 Gasification Reactors

Like pyrolysis reactors, a broad range of reactor types were designed and built for gasification based on the type of feedstock and gasification temperature. The different types of gasifiers can be classified into three categories: moving-bed reactor, fluidized-bed reactor, and entrained-flow reactor. Each type of gasifiers has its own characteristics which listed in Table 2.3 [58].

Table 2.3. Characteristics of different categories of gasifiers

category	**Moving-bed**		**Fluidized-bed**		**Entrained-flow**
Ash condition	Dry bottom	slagging	Dry ash	agglomerating	slagging
Typical processes	Lurgi	BGL	Winkler, HTW, KBR, CFB, HRL	KRW, U-Gas	KT, Shell, GEE, E-Gas, Siemens, MHI, PWR
Feed characteristics					
size	6-50 mm	6-50 mm	6-10 mm	6-10 mm	< 100 µm
Acceptability of caking coal	Yes (with stirrer)	Yes (with stirrer)	Possibly	yes	yes
Preferred coal rank	any	high	Low	any	any
Operating characteristics					
Outlet gas temperate	Low (425-650 ºC)	Low (425-650 ºC)	Moderate (900-1050 ºC)	Moderate (900-1050 ºC)	High (1250-1600 ºC)
Oxidant demand	Low	Low	moderate	moderate	High
Steam demand	High	low	moderate	moderate	Low
Other characteristics	Hydrocarbons in gas	Hydrocarbons in gas	Lower carbon conversion	Lower carbon conversion	Pure gas, high carbon conversion

In a typical updraft (counter-current) gasifier which is a type of moving-bed reactor, the feedstock is poured from the top and the produced gas will be captured from the top as well. Steam, air, or oxygen (gasifying agents) enters the gasifier from the bottom and moves upward contacting the hot descending fuel and ash. The released heat from combustion of fuel raises the temperature to the ignition point and is used for gasification.

The heated upward-moving gas along the descending solid particles take part into another exothermic reaction (partial combustion) and produce carbon monoxide. The gaseous products of combustion zone moves upward where they meet the char from the upper bed and gasification reactions take place [59]. The residual heat capacity of the rising hot gas creates a pyrolysis zone where the feedstock decomposes to non-condensable, condensable gases, and char. The mixture

gas products of both gasification and pyrolysis then dries the raw feedstock at the topmost zone of the reactor. As the thermal energy for drying, pyrolysis and gasification is provided by the combustion at the bottom of the gasifier, this kind of design can also be called flaming pyrolysis.

In a typical downdraft gasifier (co-current), the regions where pyrolysis, gasification, and combustion occur are different from the updraft gasifiers. Here gasifying agents enter the gasifier from the lower part of the reactor and take part in combustion and pyrolysis reactions. The downward moving hot produced gas then reacts with the remaining hot char through the gasification reactions. However, this type of gasifiers have some advantages in producing a tar-free syngas, but they are low in energy content. Hanaoka et al. [60] investigated the effects of CO_2 and O_2 concentrations in the gasifying agent and the feeding rate on the gasification of an aquatic biomass. An augmentation in the syngas content was reported using CO_2/O_2 as the gasifying agent. Using CO_2 can enhance the conversion of char through the partial oxidation, producing CO at the cost of H_2 reduction in syngas composition. On the other hand, they showed that increasing O_2 can result in more H_2. The reduction in syngas was observed by reducing the feeding rate but the conversion to gas remained constant. The effects of water adding and feedstock composition on gasification performance was investigated by Guo et al. [61] who applied a non-catalytic partial oxidation technology under typical temperature at 1050-1100 ºC.

In a typical fluidized-bed reactor air is blown from the bottom into a bed of sand, providing sufficient velocity to keep them in a suspension state. As soon as sufficiently high temperature is obtained, biomass feedstock is fed from the top or side. Biomass particles immediately mix with bed materials and reach the reactor temperature. At the beginning, pyrolysis occurs, followed by gasification and tar-conversion reactions in the gas phase. Any tar released moves up in the bed

with gas products. The advantages of fluidized-bed reactor include its ability to deal with lots of different feedstock without the need of pre-processing and its ease of temperature controlling.

In an entrained-flow gasifier, the feedstock and gasifying agent are fed co-currently from the top of the reactor, resulting in high degree of mixing. Rapid feedstock conversion is a direct result of high pressure and temperature conditions which induce an extremely turbulent flow inside the gasifier. This type of gasifier gives the highest amount of gaseous products due to its low residence time (in the order of few seconds). However, it has the highest carbon conversion among the other gasifiers, but its high temperature reaction, shortens the life of system components.

Along with experimental studies on gasification, numerical analysis of gasifiers can be useful in understanding the gasification mechanism and improving the gasification yields. Unlike numerous experimental works, numerical studies on gasification are still unique and untouched except some attempts [62-64]. Umeki et al. [65] numerically studied the high temperature steam gasification and compared their simulation with experimental data of a demonstration-scale gasifier. They found that among the main reactions taking place in the gasifier, the char gasification and water-gas shift play major roles in predicting the syngas composition.

Among all the experimental and numerical studies, no one has studied the gasification of bio-oil. In the next section we will review fuel spray and vaporization that are relevant to bio-oil gasification.

2.4 Spray Modeling

In this study bio-oil is sprayed through a nozzle, atomizes, vaporizes and finally reacts with the gasifying agent to produce syngas. In order to simulate these processes, a crucial step is the simulation of spray and vaporization. Spray may seem a common process but the physics describing spray dynamics, droplet break up and atomization is among the most complex areas.

Considering a solid-cone spray, the liquid spray can be divided into several different regions. Starting from the nozzle exit, liquid fuel can break up into ligaments and droplets. The liquid breakup includes primary and secondary breakup. The primary break up can be induced by turbulence within the liquid phase, implosion of cavitation bubbles, and aerodynamics forces acting on the liquid jet [66]. A high level of turbulence caused by high-velocity drops can break up the liquid jet as it exits the nozzle. On the other hand, cavitation bubbles can form inside the nozzle. As this bubbles leave the nozzle, they will implode and take part in disintegration of the spray. The high relative velocity between the fuel spray and the gas phase can develop surface disturbances (aerodynamic forces) to induce breakup. The contribution of each mechanism to the spray breakup depends on various parameters, such as relative velocity between liquid and gas, density ratio, viscosity and liquid surface tension. The breakup regions can be classified according to various non-dimensional numbers, including Reynolds, Weber, and Ohnesorge [67].

$$\mathrm{Re} = \frac{\rho v_{inj} d_{noz}}{\mu} \tag{2.17}$$

$$We = \frac{\rho v_{inj}^2 d_{noz}}{\sigma} \tag{2.18}$$

$$Z = \frac{\mu}{\sqrt{\rho \sigma d_{noz}}} \tag{2.19}$$

Blob model is the simplest and most popular approaches to describe the injection conditions of droplets. This model assumes a uniform spherical droplet with diameter equal to that of nozzle at the time of injecttion. The spherical droplets are subjected to aerodynamics-induced secondary breakup. Kuensberg et al. [68] enhanced the blob model by taking into account the reduction of the nozzle cross section due to cavitation. Their enhanced model modifies the injection particle diameter and the particle injection velocity by considering cavitation inside the nozzle [69].

Breakup of the injected liquid induced by relative velocity between gas and liquid phases was introduced and modeled by Rietz [70]. This model is widely applied in primary and secondary breakup models. The liquid surface of a cylindrical jet of radius *a* which penetrates into a stationary incompressible gas medium will be subjected to a number of infinitesimal perturbations. Considering η_0 as the initial perturbation amplitude and λ as the spectrum wavelengths, the growth in amplitudes caused by liquid-gas interactions can be defined as

$$\eta(t) = R(\eta_0 \exp[ikx + \omega t]) \tag{2.20}$$

$$\omega = \omega_r + i\omega_i \tag{2.21}$$

However, the perturbations of different wavelengths will superimpose each other, only the fastest growing perturbation by growth rate Ω and corresponding wavelength Λ causes the breakup. Applying the curve-fits of numerical solutions, Reitz [70] obtained the simplified expression of the maximum growth rate and corresponding wavelength as

$$\frac{\Lambda}{a} = 9.02\frac{\left(1+0.45\times Z^{0.5}\right)\left(1+0.4\times T^{0.7}\right)}{\left(1+0.87\times We_g^{1.67}\right)^{0.6}} \tag{2.22}$$

$$\Omega\left(\frac{\rho_l a^3}{\sigma}\right)=\frac{0.34+0.38\times We_g^{1.5}}{(1+Z)(1+1.4\times T^{0.6})} \tag{2.23}$$

where $Z=\frac{We_l^{0.5}}{\mathrm{Re}_l}$, $T=Z\,We_g^{0.5}$, $We_l=\frac{\rho_l U^2 a}{\sigma}$, $We_g=\frac{\rho_g U^2 a}{\sigma}$, $\mathrm{Re}_l=\frac{Ua}{\nu_l}$.

The above relations show that by increasing the gas Weber number, the growth rate augments whilst the corresponding wavelength decreases. This is in agreement with experimental studies as higher injection velocities enhance the breakup and the produce smaller droplets.

2.5 Drop Vaporization

The basic drop vaporization model for an isolated single-component drop in a stagnant environment was well studied in the literature [71-73]. By considering the heat transfer, the energy equation of a drop can be formulated as

$$4\pi r^2 k_g \frac{dT}{dr}=\dot{m}_{tot}c_{pv}(T-T_s)+\dot{m}_{tot}L(T_s)+\dot{q}_d \tag{2.24}$$

where k_g is the thermal conductivity of gas phase, and c_{pv} is the mass averaged specific heat of the fuel. In the above equation, the left hand side stands for conduction heat transfer from the environment to the drop. On the right hand side, the first term is the amount of heat transfer for heating the fuel vapor from drop surface temperature to the ambient temperature, and the second term is the amount of heat absorbed for vaporization latent heat. The last term accounts for drop internal energy that can be related with its temperature as follows

$$\dot{q}_d=\frac{4}{3}\pi R^3 \rho_L c_v \frac{dT_d}{dt} \tag{2.25}$$

By solving Eq. (2.24) and by applying the proper boundary conditions from the drop surface (at $r=R$, $T=T_s$) to infinity (at $r=\infty$, $T=T_\infty$), a simplified expression for drop vaporization rate can be written.

$$\dot{m}_{tot} = \frac{4\pi R k_g}{c_{pv}} \ln(1 + B_T) \tag{2.26}$$

B_T is the Spalding heat transfer number and is defined as

$$B_T = \frac{c_{pv}(T_\infty - T_s)}{L(T_s)} \tag{2.27}$$

Using the Spalding mass transfer number B_M ,

$$B_M = \frac{y_s - y_\infty}{1 - y_s} \tag{2.28}$$

we can introduce the following correlation

$$1 + B_T = (1 + B_M)^{\varphi} \tag{2.29}$$

where $\varphi = \frac{c_{pv}}{c_{pg}} \frac{1}{Le}$, c_{pg} is the specific heat of the ambient gas, and Le is the Lewis number which is defined as

$$Le = \frac{k_g}{c_{pg} \rho D_{l,g}} \tag{2.30}$$

Assuming a drop without vaporization, the amount of heat transfer to the drop surface can be calculated using the convective heat transfer coefficient. For non-convection situations, Nusselt number is equal to 2, and the amount of heat transfer to the non-vaporized drop can be calculated as

$$\dot{q}_{s,non-vap} = 4\pi R^2 \frac{k_g}{R}(T_\infty - T_s) \tag{2.31}$$

Using Eqs. (2.26) and (2.27), the amount of heat transferred to the drop surface with or without evaporation can be formulated as

$$\dot{q}_s = \dot{q}_{s,non-vap} \frac{z}{e^z - 1} \tag{2.32}$$

z is defined as

$$z = \frac{\dot{m}_{tot} c_{pv}}{4\pi k_g R} \tag{2.33}$$

Eq. (2.32) shows the correlation of heat transfer rates to the drop surface in vaporization and non-vaporization situations. This analogy can be used to relate the corresponding Nusselt number of a vaporizing drop to a non-vaporizing one as

$$Nu = Nu_0 \frac{z}{e^z - 1} = Nu_0 \frac{\ln(1 + B_T)}{B_T} \tag{2.34}$$

where Nu_0 can be related to Reynolds and Prandtl number as

$$Nu_0 = 2 + 0.6 \mathrm{Re}^{0.5} \mathrm{Pr}^{\frac{1}{3}} \tag{2.35}$$

Consequently, under the forced convection situation, the vaporization rate based on Nusselt number can be written as

$$\dot{m}_{tot} = \frac{2\pi R k_g}{c_{pv}} Nu\, B_T = \frac{2\pi R k_g Nu_0}{c_{pv}} \ln(1 + B_T) \tag{2.36}$$

CHAPTER 3. METHODOLOGY

This study uses KIVA-3V as the baseline CFD code to solve the governing equations. KIVA is as Fortran-based CFD code developed by Los Alamos National Laboratory to analyze a transient, three-dimensional, multiphase chemically reacting flow with sprays by using an Arbitrary Lagrangian Eulerian (ALE) and finite volume technique. The code was basically designed for analyzing internal combustion engine problems, and it can be used for a variety of problems with sprays and chemical reactions.

3.1 Governing Equations

The continuity equation for species *m* is

$$\frac{\partial \rho_m}{\partial t} + \nabla.\left(\rho_m U\right) = \nabla.\left[\rho D \nabla\left(\frac{\rho_m}{\rho}\right)\right] + \dot{\rho}_m^c + \dot{\rho}^S \delta_{m1} \tag{3.1}$$

where ρ_m is the mass density of species *m*, ρ the total mass density, and *U* the fluid velocity. Fick's Law diffusion is used with a single diffusion coefficient of *D*. Species 1 is the species of which the spray droplets are composed, and δ is the Dirac delta function. By summing Eq.(3.1) over all species, the total fluid density equations can be obtained as

$$\frac{\partial \rho}{\partial t} + \nabla.\left(\rho U\right) = \dot{\rho}^S \tag{3.2}$$

since mass is conserved in chemical reactions.

The momentum equation for fluid mixture is

$$\frac{\partial\left(\rho U\right)}{\partial t} + \nabla.\left(\rho U^2\right) = -\frac{1}{a^2}\nabla p - A_0 \nabla\left(\frac{2}{3}\rho k\right) + \nabla.\sigma + F^S + \rho g \tag{3.3}$$

where p is the fluid pressure. The dimensionless quantity *a* is used in conjunction with the Pressure Gradient Scaling (PGS) Method. This is a method for enhancing computational efficiency in low Mach number flows, where the pressure is nearly uniform. The user may opt not to use the PGS method, in which case *a*=1.

In Eq.(3.3) the quantity A_0 is zero in laminar calculations and unity when one of the turbulence models is used. The internal energy equation is

$$\frac{\partial(\rho I)}{\partial t}+\nabla.(\rho U\, I)=-p\nabla.U+(1-A_0)\sigma:\nabla U-\nabla.J+A_0\rho\varepsilon+\dot{Q}^C+\dot{Q}^S \tag{3.4}$$

where *I* is the specific internal energy, exclusive of chemical energy.

When one of the turbulence models are in use ($A_0=1$), two additional transport equations are solved for the turbulent kinetic energy *k* and its dissipation rate ε as

$$\frac{\partial\rho k}{\partial t}+\nabla.(\rho Uk)=-\frac{2}{3}\rho k\nabla.U+\sigma:\nabla U+\nabla.\left[\left(\frac{\mu}{\mathrm{Pr}_k}\right)\nabla k\right]-\rho\varepsilon+\dot{W}^S \tag{3.5}$$

and

$$\frac{\partial\rho\varepsilon}{\partial t}+\nabla.(\rho U\varepsilon)=-\left(\frac{2}{3}c_{\varepsilon_1}-c_{\varepsilon_3}\right)\rho\varepsilon\nabla.U+\nabla.\left[\left(\frac{\mu}{\mathrm{Pr}_k}\right)\nabla\varepsilon\right]+\frac{\varepsilon}{k}\left[c_{\varepsilon_1}\sigma:\nabla U-c_{\varepsilon_2}\rho\varepsilon+c_s\dot{W}^S\right] \tag{3.6}$$

These are standard k-ε equations with some added terms. The source term $\left(c_{\varepsilon_3}-\frac{2}{3}c_{\varepsilon_1}\right)\nabla.U$ in the ε-equation accounts for length scale changes when there is velocity dilation. Source terms involving the quantity $\dot{W}^S$ arise due to the interaction with the spray. The quantities c_{ε_1}, c_{ε_2}, c_{ε_3}, Pr_k, and Pr_ε are constants whose values are determined from experiments and theoretical considerations. Standard values of these are used.

Solving the essential dynamics of spray and its interactions with a gas is an extremely complicated problem. To calculate the mass, momentum, and energy exchange between the spray and the gas, one must account for a distribution of drop sizes, velocities, and temperatures. In many sprays, drop Weber numbers are larger than unity, and drop oscillations, distortios, and breakup must be considered. Drop collisions and coalescences have also been found to be important in many engine sprays. The mathematical formulations of drop collision and coalescence are based on the original KIVA-3V models [74]. The drop breakup is simulated using the KH-RT breakup model introduced by Reitz [70].

3.2 Multi-component Drop Vaporization

Bio-oil is a multi-component fuel consisting of many different species. The multi-component vaporization theory shares the same fundamentals as the single-component vaporization theory with modifications for considering vaporization of multiple components simultaneously.

Considering a single bio-oil drop surrounded by higher temperature ambient gas, the vaporization rate of an individual component (*i*) can be expressed as

$$\frac{\dot{m}_i}{4\pi r^2} = -D_{i,g}\rho\frac{dy_i}{dr} + y_i\frac{\dot{m}_{tot}}{4\pi r^2} \tag{3.7}$$

In the above equation, $\dot{m}_i$ is the vaporization rate of component (*i*) which is related to binary diffusion of component (*i*) into the ambient gas and also the overall vaporization rate ($\dot{m}_{tot}$) of the drop. *r* is the drop radius at the current time, and $D_{i,g}$ is the binary diffusivity coefficient between the component (*i*) and ambient gas. ρ is the mass averaged density of droplet and y_i is the mass fraction of component (*i*).

By introducing the vaporization fraction rate as

$$\varepsilon_i = \frac{\dot{m}_i}{\dot{m}_{tot}}, \tag{3.8}$$

one can obtain the following equation

$$\sum_{i=1}^{n} \varepsilon_i = 1, \tag{3.9}$$

Assuming constant total gas density and binary diffusivity, Eq. (3.7) can be solved by integrating from the drop surface to infinity. The simplified equation representing the vaporization rate of each component can be written as

$$\dot{m}_i = \dot{m}_{tot}\varepsilon_i = 4\pi R\rho\varepsilon_i D_i \ln\left(1 + B_{M,i}\right), \tag{3.10}$$

where $B_{M,i}$ is the Spalding mass transfer number of component (*i*) defined as

$$B_{M,i} = \frac{y_{i,s} - y_{i,\infty}}{\varepsilon_i - y_{i,s}}, \tag{3.11}$$

where subscript *s* and ∞ denoted the corresponding values at drop surface and infinity, respectively. Eqs.(3.10) and (3.11) show that the vaporization rate of a component can be obtained by the vapor mass fraction at drop surface and infinity. In order to find the vapor mass fraction at the drop surface, the phase equilibrium equation was used as follow

$$Y_{i,s} = X_{i,s}\frac{P_{v,i}\left(T_s\right)}{P_{amb}}, \tag{3.12}$$

where $Y_{i,s}$ is the mole fraction of component (*i*) in gas phase while $X_{i,s}$ is the mole fraction in liquid phase. $P_{v,i}$ is the vapor pressure of the component at drop surface temperature, and P_{amb} is the ambient pressure.

Using Eq.(3.10) for any two components of the multi-component fuel, the following equation can be obtained

$$\left(1+B_{M,i}\right)^{D_{i,g}} = \left(1+B_{M,j}\right)^{D_{j,g}} \tag{3.13}$$

Eq.(3.13) provides n-1 equation for a n-component fuel. Using Eq.(3.13) along with Eq.(3.9) the number of unknown and equations will be equal and the vaporization rate of each component can be obtained.

The vaporization model discussed here is for a stagnant multi-component drop, which can be extended for a moving drop. The theory of a moving single drop was discussed in the previous chapter, and here the final result for vaporization rate is presented

$$\dot{m}_i = 2\pi R\rho\varepsilon_i Sh_{i,o} D_i \ln\left(1+B_{M,i}\right) \tag{3.14}$$

where $Sh_{i,o}$ is the average Sherwood number for a sphere and is related to Reynolds and Schmidt numbers as

$$Sh_{i,o} = 2.0 + 0.6\,\mathrm{Re}^{\frac{1}{2}}\, Sc_i^{\frac{1}{3}} \tag{3.15}$$

3.3 Chemical Reaction Model

The gasification process occurs at relatively high temperature and thermodynamic equilibrium is expected at the exit of the reactor, as suggested by experimental results. Therefore, a thermodynamic equilibrium approach is used to predict the final product composition to avoid the use of complex gasification kinetic mechanisms.

Reaching the state of equilibrium does not happen all of a sudden and the temporal evolution should be considered. In the present model, the time rate of change of the mass fraction of species *m*, due to conversion from one chemical species to another, is given by [75]

$$\frac{dY_m}{dt} = -\frac{Y_m - Y_m^{eq}}{\tau_c} \tag{3.16}$$

Y_m is the mass fraction of species *m*, Y_m^{eq} is the local and instantaneous thermodynamic equilibrium value of the mass fraction, and τ_c is the characteristic time, which will be defined later. The characteristic time can be different for each species, but in this study we assume that it is the same for all species. Seven active species are considered in this study including, fuel, oxygen (O_2), nitrogen (N_2), carbon dioxide (CO_2), carbon monoxide (CO), hydrogen (H_2), and water (H_2O). Except N_2, the other six species are considered as the active species in calculating the instantaneous thermodynamic equilibrium values.

One of the important aspect of this model is to properly define and formulate the characteristic time τ_c. This timescale is derived from laminar flame chemistry. The laminar chemistry timescale is derived from the correlated one-step reaction rate for typical hydrocarbon fuels [76],

$$Rate = A[Fuel]^m [O_2]^n \exp\left(-\frac{E}{RT}\right) \tag{3.17}$$

At the equilibrium state, there is no fuel remaining, therefore $Y_{fuel}^{eq} = 0$. Equating Eqs.(3.16) and (3.17), knowing that $Rate = \frac{dY_m}{dt}$, the reaction timescale can be obtained as

$$\tau_c = A^{-1}[Fuel]^{1-m}[O_2]^{-n} \exp\left(\frac{E}{RT}\right) \tag{3.18}$$

3.4 Chemical Equilibrium

The overall chemical reaction of a hydrocarbon based fuel can be written as

$$C_\alpha H_\beta O_\gamma N_\delta + \frac{a_s}{\varphi}(O_2 + 3.76N_2) \rightarrow n_1 CO_2 + n_2 H_2O + n_3 N_2 + n_4 O_2 + n_5 CO + n_6 H_2 + n_8 O + n_9 OH + n_{10} NO + ... \tag{3.19}$$

where φ is the equivalence ratio and

$$a_s = \alpha + \frac{\beta}{4} - \frac{\gamma}{2} \tag{3.20}$$

The left hand side of Eq.(3.19) is known and the right hand side is where the unknowns lie. The first step in finding the unknowns (n_i) is the mass balance of different atoms

$$C: \ \alpha = (x_1 + x_2)N \tag{3.21}$$

$$H: \ \beta = (2x_2 + 2x_6 + x_7 + x_9)N \tag{3.22}$$

$$O: \ \gamma + \frac{2a_s}{\varphi} = (2x_1 + x_2 + 2x_4 + x_5 + x_8 + x_9 + x_{10})N \tag{3.23}$$

$$N: \quad \delta + \frac{7.52 a_s}{\varphi} = (2x_3 + x_{10})N \tag{3.24}$$

where N is the total number of moles and x_i's are the corresponding mole fraction and sum of them would be equal to unity.

$$\sum_{i=1}^{10} x_i = 1 \tag{3.25}$$

In order to find a solution for 11 unknowns we need six more equations. These six additional equations will be provided by six equilibrium reactions. These reactions include the dissociation of hydrogen, water, carbon dioxide, carbon monoxide, and equilibrium OH and NO.

$$\frac{1}{2} H_2 \Leftrightarrow H \qquad K_1 = \frac{x_7 P^{0.5}}{x_6^{0.5}} \tag{3.26}$$

$$\frac{1}{2} O_2 \Leftrightarrow O \qquad K_2 = \frac{x_8 P^{0.5}}{x_4^{0.5}} \tag{3.27}$$

$$\frac{1}{2} H_2 + \frac{1}{2} O_2 \Leftrightarrow OH \qquad K_3 = \frac{x_9}{x_4^{0.5} x_6^{0.5}} \tag{3.28}$$

$$\frac{1}{2} N_2 + \frac{1}{2} O_2 \Leftrightarrow NO \qquad K_4 = \frac{x_{10}}{x_4^{0.5} x_3^{0.5}} \tag{3.29}$$

$$CO + \frac{1}{2} O_2 \Leftrightarrow CO_2 \qquad K_5 = \frac{x_1}{x_5 x_4^{0.5} P^{0.5}} \tag{3.30}$$

$$CO + H_2O \Leftrightarrow CO_2 + H_2 \qquad K_6 = \frac{x_6 x_1}{x_2 x_5} \tag{3.31}$$

In the above equations the unit of pressure is atm and the equilibrium constants (K_i) are functions of temperature. It must be noted that the above equations are highly non-linear and special treatment should be taken to converge to the correct solution. The Newton-Raphson

method is mainly used to solve the coupled nonlinear equations. Aithal [77] developed a fast, robust equilibrium chemistry solver using the modified Newton-Raphson method.

3.5 Evaluating Bio-oil Properties

Bio-oil is a complex mixture consisting of different types of components. The thermophysical properties of most of these components are still unknown due to lack of experimental data. One method, which is widely used in calculating the thermophysical properties of new species, is Joback method which is a group contribution method. In this method the basic structural information of a chemical molecule is used and eleven common and important thermophysical properties of the molecule will be obtained. These eleven properties can be listed and calculated using the following formulations

Normal Boiling	$T_b = 198 + \sum T_{b,i}$	(3.32)
Melting Point	$T_m = 122.5 + \sum T_{m,i}$	(3.33)
Critical Temperature	$T_c = T_b \left[0.584 + 0.965 \sum T_{c,i} - \left(\sum T_{c,i} \right)^2 \right]^{-1}$	(3.34)
Critical Pressure	$P_c = \left[0.113 + 0.0032 N_A - \sum P_{c,i} \right]^{-2}$	(3.35)
Critical Volume	$V_c = 17.5 + \sum V_{c,i}$	(3.36)
Heat of Formation	$H_{form} = 68.29 + \sum H_{form,i}$	(3.37)
Gibbs Energy	$G_{form} = 53.88 + \sum G_{form,i}$	(3.38)
Heat Capacity	$C_p = \sum a_i - 37.93 + \left(\sum b_i + 021 \right) T + \left(\sum c_i - 3.91 \times 10^{-4} \right) T^2 + \left(\sum d_i + 2.06 \times 10^{-7} \right) T^3$	(3.39)
Heat of Vaporization	$\Delta H_{vap} = 15.3 + \sum H_{vap,i}$	(3.40)
Heat of Fusion	$\Delta H_{fus} = -0.88 + \sum H_{fus,i}$	(3.41)
Dynamic Viscosity	$\eta_L = M_w \exp\left[\left(\sum \eta_a - 597.82 \right) / T + \sum \eta_b - 11.202 \right]$	(3.42)

Table 3.1 shows the group contributions and their corresponding constants for non-ring groups

Table 3.1. Joback group contribution and corresponding constants

Group	T_c	P_c	T_b	T_m	H_{form}	G_{form}	a	b	c	d
	Critical State data		Temperatures of Phase Transitions		Chemical Caloric Properties		Ideal Gas Heat Capacities			
Non-ring Groups										
$-CH_3$	0.0141	−0.0012	23.58	−5.10	−76.45	−43.96	1.95E+1	−8.08E−3	1.53E−4	−9.67E−8
$-CH_2-$	0.0189	0.0000	22.88	11.27	−20.64	8.42	−9.09E−1	9.50E−2	−5.44E−5	1.19E−8
>CH-	0.0164	0.0020	21.74	12.64	29.89	58.36	−2.30E+1	2.04E−1	−2.65E−4	1.20E−7
>C<	0.0067	0.0043	18.25	46.43	82.23	116.02	−6.62E+1	4.27E−1	−6.41E−4	3.01E−7
$=CH_2<$	0.0113	−0.0028	18.18	−4.32	−9.630	3.77	2.36E+1	−3.81E−2	1.72E−4	−1.03E−7
=CH-	0.0129	−0.0006	24.96	8.73	37.97	48.53	−8.00	1.05E−1	−9.63E−5	3.56E−8
=C<	0.0117	0.0011	24.14	11.14	83.99	92.36	−2.81E+1	2.08E−1	−3.06E−4	1.46E−7
=C=	0.0026	0.0028	26.15	17.78	142.14	136.70	2.74E+1	−5.57E−2	1.01E−4	−5.02E−8
≡CH	0.0027	−0.0008	9.20	−11.18	79.30	77.71	2.45E+1	−2.71E−2	1.11E−4	−6.78E−8
≡C-	0.0020	0.0016	27.38	64.32	115.51	109.82	7.87	2.01E−2	−8.33E−6	1.39E-9

After obtaining the critical thermo-physical properties, e.g., critical pressure, temperature, etc., Pitzer's expansion was used to find the vapor pressure at different temperatures.

$$\ln\left(P_{vapor}\right)=f^{(0)}\left(T_r\right)+\omega f^{(1)}\left(T_r\right) \tag{3.43}$$

where $f^{(0)}$ and $f^{(1)}$ are correlations [78, 79] expressing as

$$f^{(0)}=5.92714-\frac{6.09648}{T_r}-1.28862\ln\left(T_r\right)+0.169347T_r^6 \tag{3.44}$$

$$f^{(1)}=15.2518-\frac{15.6875}{T_r}-13.4721\ln\left(T_r\right)+0.43577\,T_r^6 \tag{3.45}$$

$$\omega=-\log\left(P_{vapor}\big|_{T_r=0.7}\right)-1 \tag{3.46}$$

In the above equations, T_r is the a non-dimensional value defined as

$$T_r=\frac{T}{T_c} \tag{3.47}$$

Using the same parameter (T_r), latent heat can be calculated through Lielmez's method [79]

$$L=L_b\frac{T_r}{T_{br}}\frac{X+X^q}{1+X^p}, \tag{3.48}$$

where X is defined by

$$X=\frac{T_{br}}{T_r}\frac{1-T_r}{1-T_{br}} \tag{3.49}$$

Subscript *b* refers to the normal boiling point. L_b can be estimated using Riedel method as

$$L_b = 1.093RT_c\left[T_{br}\frac{\ln(P_c)-1.013}{0.930-T_{br}}\right]. \tag{3.50}$$

CHAPTER 4. RESULTS AND DISCUSSION

Bio-oil gasification is simulated using the updated KIVA-3V code to predict the syngas composition and the evolution of products at different operating conditions. The gasifier in this study has an injector on the top to inject bio-oil and oxygen into the gasifier. The nozzle is designed in a way to help atomize and vaporize bio-oil drops. This gasifier [81] is located at Iowa State University and is a cylindrical reactor with 3.3 cm in diameter and 101 cm in length. A cross-sectional view of the gasifier assembly is shown in Figure 4.1.

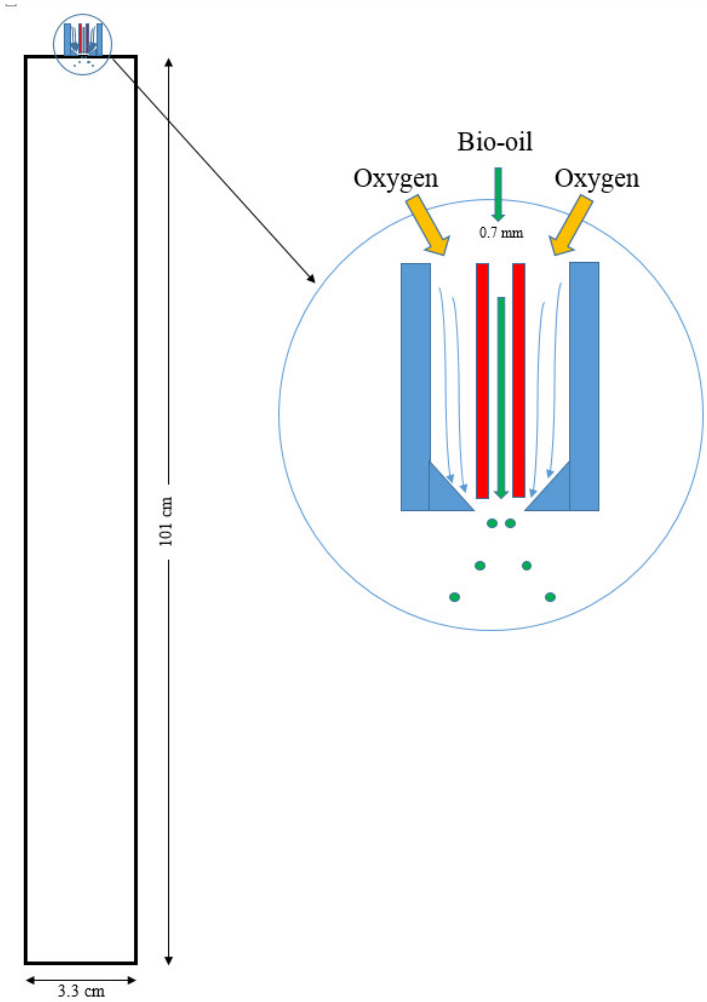

Figure 4.1. Cross-sectional view of the gasifier assembly

This gasifier is designed to operate at pressures up to 200 psig. The operating temperature is fixed at 850 ºC by wall heating. The reactor gasification capacity is to gasify 0.132 g/s of fuel. The injector sprays both fuel and gasifying agent (oxygen and trace of nitrogen) simultaneously. The schematic of the injector is shown in Figure 4.2. The nozzle diameter is 0.7 mm.

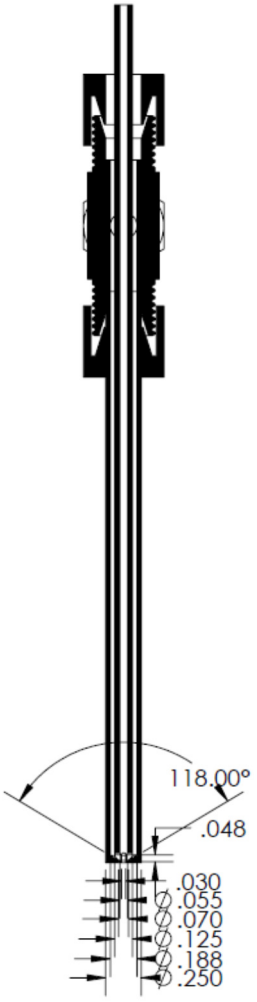

Figure 4.2. Schematic of the injector

The gasifier operating conditions and its characteristics are listed in Table 4.1. Equivalence ratio is defined as the ratio of “actual air-fuel mass ratio” to “stoichiometric air-fuel mass ratio.” Note that this definition is commonly used in the gasification industry and it is the opposite of the definition used in the combustion industry. In this study gasification is usually operated at an equivalence ratio of 0.25, which is a fuel rich condition with only 25% theoretical air to produce incomplete combustion. Both methanol and bio-oil are used as the feedstock. Methanol is used at the shake-down stage of the gasifier testing and operation, prior to bio-oil experiments.

Table 4.1. Gasifier characteristics and operating conditions

Reactor Length (cm)	101 (cm)
Reactor Diameter (cm)	3.3 (cm)
Injector Diameter (mm)	0.7 (mm)
Fuel mass flow rate (gr/s)	0.132 g/s
Equivalence ratio (Φ)	0.25, 0.3
Operating Temperature (ºC)	850 (ºC)
Operating Pressure (psig)	0, 100, 200 (psig)
Fuel Type	Methanol, Bio-oil

As the reactor is a cylinder and the injector is located at the center, a two-dimensional domain is used for numerical simulation. At the first step, the vaporization and gasification of methanol is simulated. Results are compared with the experimental data in order to validate the present model. Then, simulation of bio-oil gasification will be conducted.

4.1 Methanol Gasification

4.1.1 Methanol vaporization

In this section methanol spray and vaporization history inside the gasifier was modeled. A proper and high performance gasification process can be achieved if the liquid fuel vaporizes and properly mixes with the gasifying agent to form a homogenous mixture. Figure 4.3 shows the history of methanol spray and vapor inside the gasifier for the first 0.1 second of its injection. The interval of the results shown in Figure 4.3 is every 0.006 sec from left to right.

As depicted in Figure 4.3, the moment methanol is injected into the gasifier, it starts to vaporize and mix with air. As more liquid fuel vaporizes, the gas phase density increases, and as a result, the vaporization rate decreases. Therefore, subsequent drops have to move downstream to completely vaporize. Some drops hit the wall and eventually vaporize. As can be seen, the vapor mole fraction is relatively high near the wall and central regions (red color). Numerical simulation shows that the present geometry and operating conditions can result in a reasonably homogenous mixture for gasification.

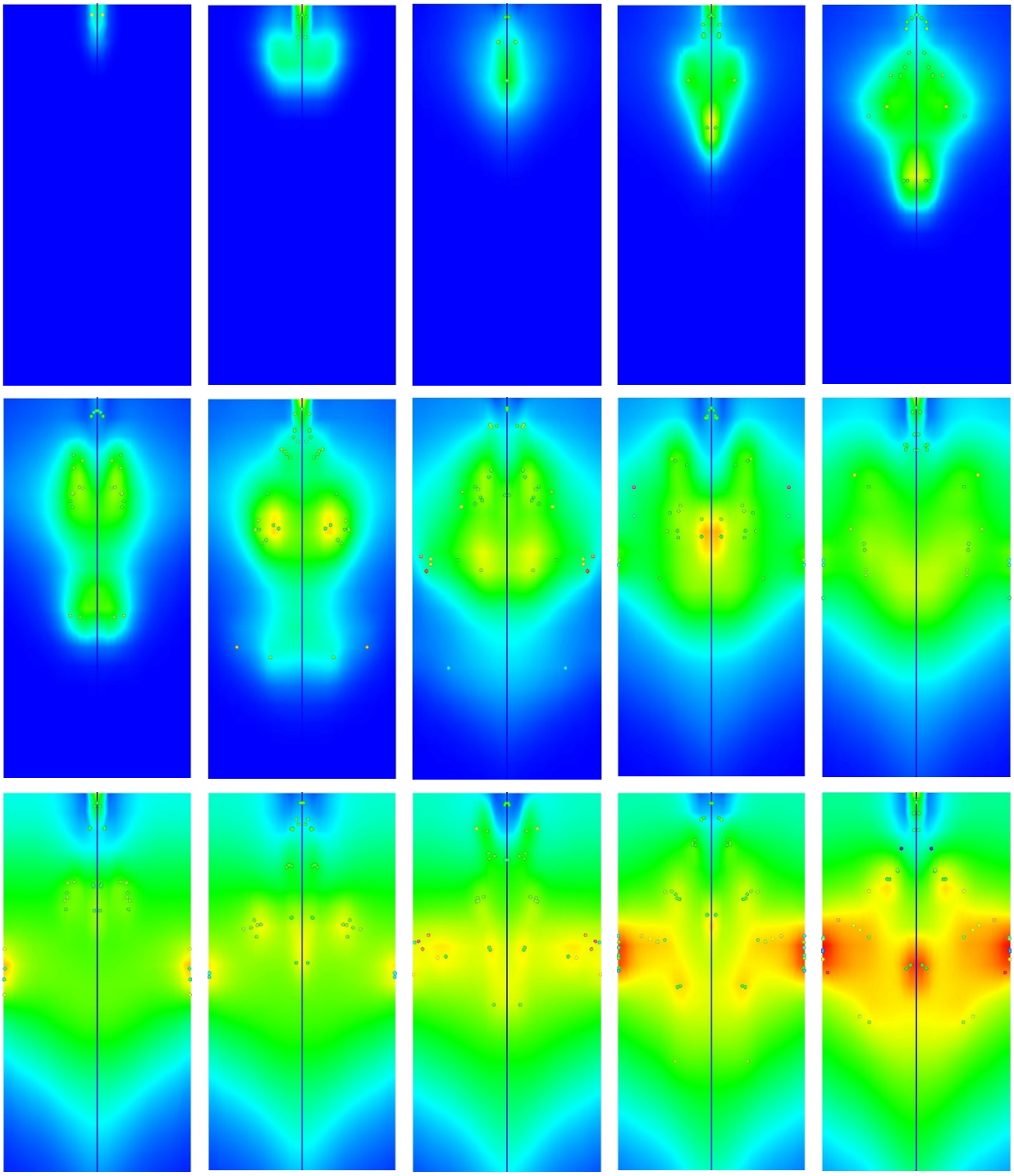

Figure 4.3. Spray and vapor distribution of methanol during the first 0.1 s of the injection. Fuel mass flow rate is fixed at 0.132 g/s with 25% theoretical air. Pressure and temperature are fixed at 0 psig and 850 ºC, respectively. The time interval between graphs is 6 ms. Only the top 7 cm of gasifier is illustrated in vertical direction.

4.1.2 Chemical reaction formulation

In the simulation, the rates of chemical reactions leading to syngas production are controlled by the following equation

$$\tau_l = A^{-1}[Fuel]^{1-m}[O_2]^{-n}\exp\left(\frac{E}{RT}\right) \tag{4.1}$$

where A is the pre-exponential constant and τ_l is the laminar time scale. In this section the effects of A, m, and n on the temporal evolution of products are presented.

Figure 4.4 to Figure 4.6 show the effect of pre-exponential constant on fuel and syngas mole fraction. As can be seen, for small values of A (0.7×10^6 ~ 0.7×10^7), reactants (fuel) and products (hydrogen and carbon monoxide) do not reach their equilibrium states. As A augments, the thermodynamic equilibrium will be obtained faster. Figure 4.7 shows the overall evolution of reactants and products over time. As fuel and oxygen react, products, including CO, H_2, H_2O, CO_2, reach their equilibrium state values.

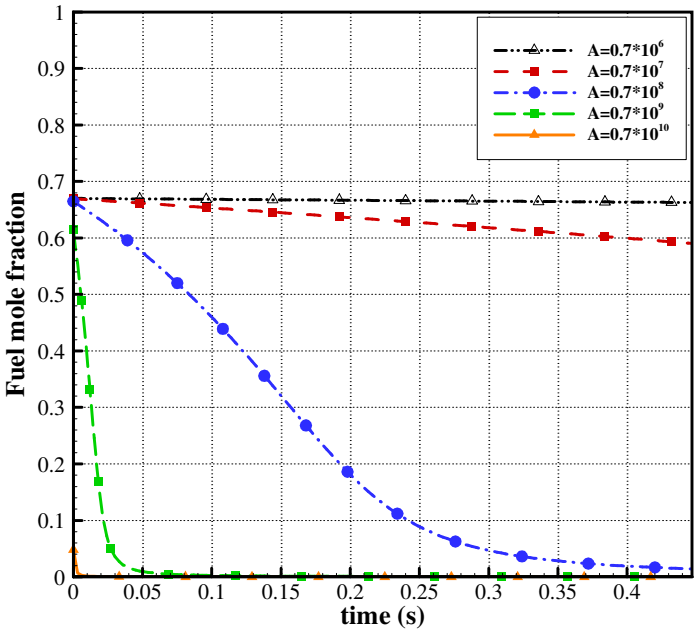

Figure 4.4. Effect of pre-exponential factor on fuel consumption

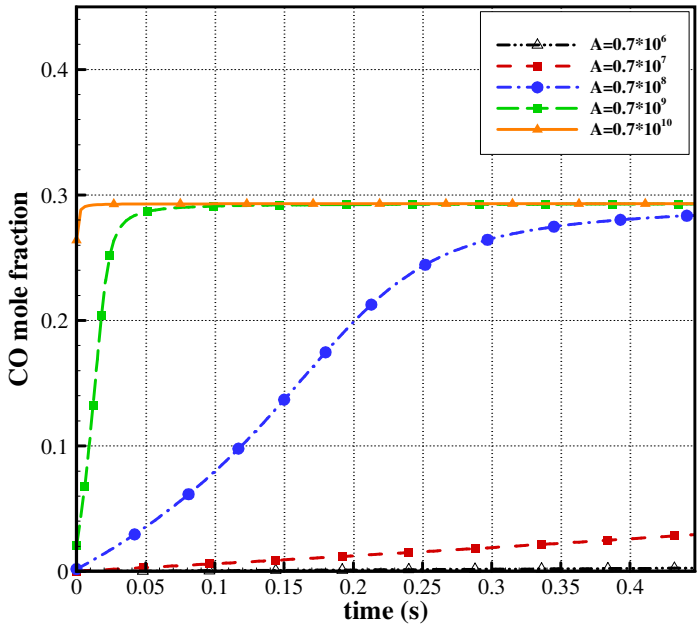

Figure 4.5. Effect of pre-exponential factor on CO production

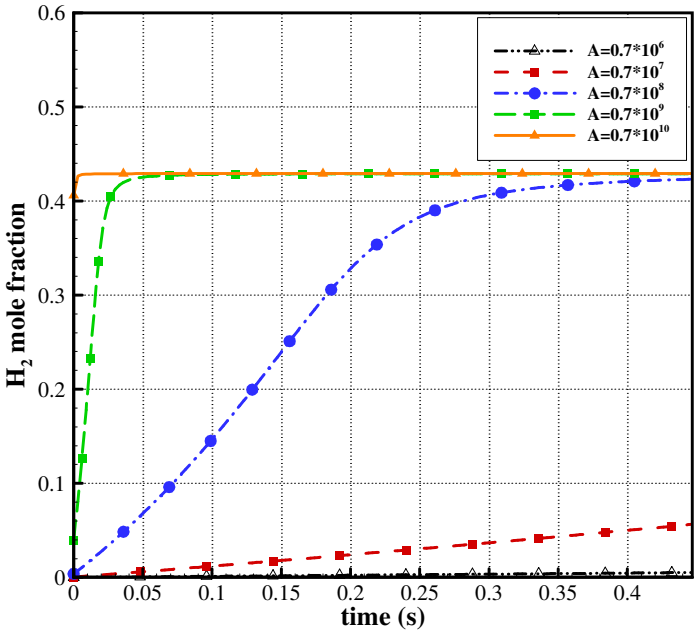

Figure 4.6. Effect of pre-exponential factor on H_2 production

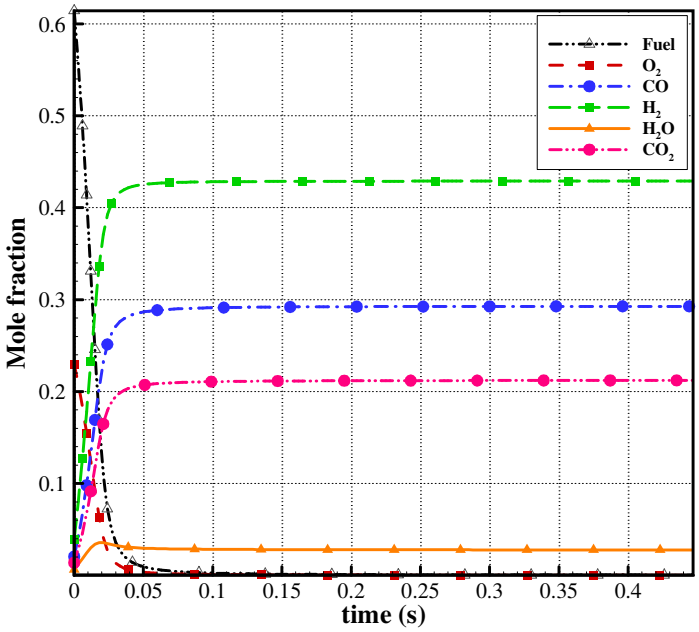

Figure 4.7. Temporal evolution of reactants and products

The effects of two other parameters, m and n are shown in Figure 4.8 and Figure 4.9. Increasing the value of m and n results in slower reactions, and the reaction is more sensitive to the variation of n. Based on what have been suggested in literature, m=0.25 and n=1.5 are chosen for this study.

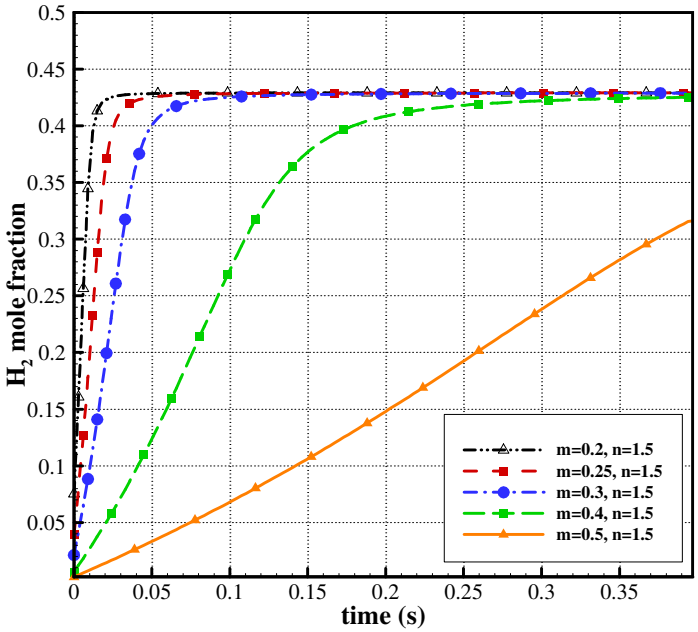

Figure 4.8. Effect of exponential coefficient m on H_2 production

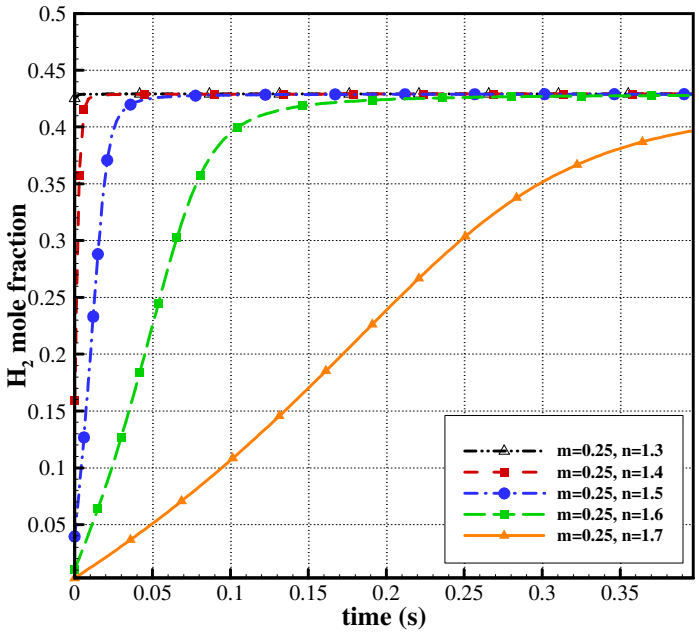

Figure 4.9. Effect of exponential coefficient n on H_2 production

4.1.3 Fuel and syngas temporal evolution

With the present models for spray, vaporization, and chemical reactions, the syngas evolution resulting from methanol gasification is obtained. Methanol mass flow rate is fixed at 0.132 g/s and the gasifier operates at atmospheric pressure and 850 ℃. Mole fractions of the fuel and products during the first 4 seconds of the simulation are displayed in Figure 4.10 to Figure 4.14. As can be seen, after spraying the fuel, it vaporizes and mixes with air. After forming a reasonable homogenous mixture, chemical reactions commence and products form downstream of the gasifier. After about 4 seconds the products reach their equilibrium state at the outlet. The fuel rich condition allows the production of hydrogen and carbon monoxide to the highest percentage, which is the goal of gasification. By comparing the hydrogen and carbon monoxide formation along the gasifier, it can be seen that carbon monoxide reaches its equilibrium state faster than hydrogen.

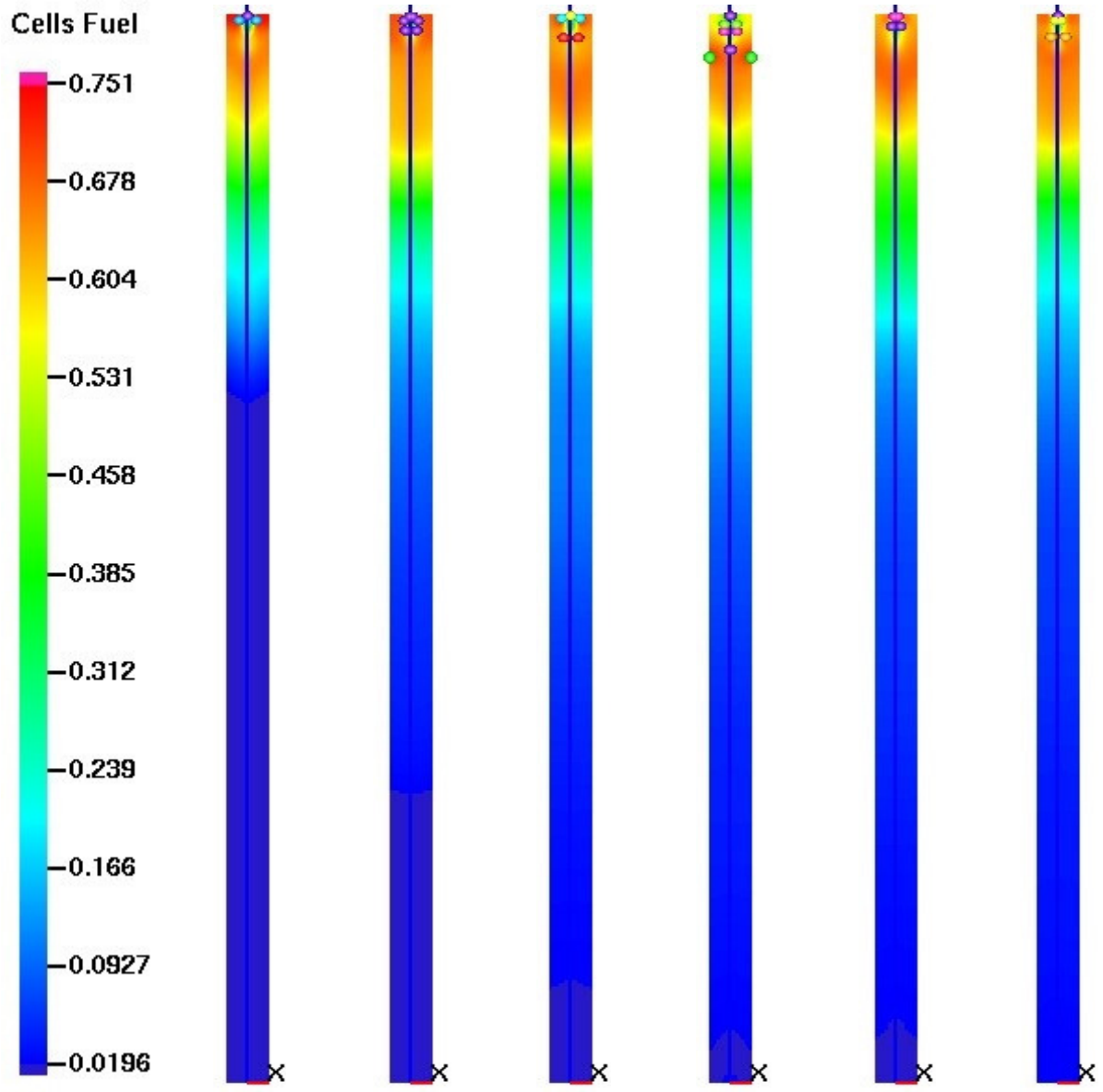

Figure 4.10. Methanol mole fraction distribution during the first 4 seconds of operation. Fuel mass flow rate is 0.132 g/s and the corresponding equivalence ratio is 0.25 at atmospheric pressure and 850 ºC. The distribution of methanol mole fraction is presented every 0.33 sec.

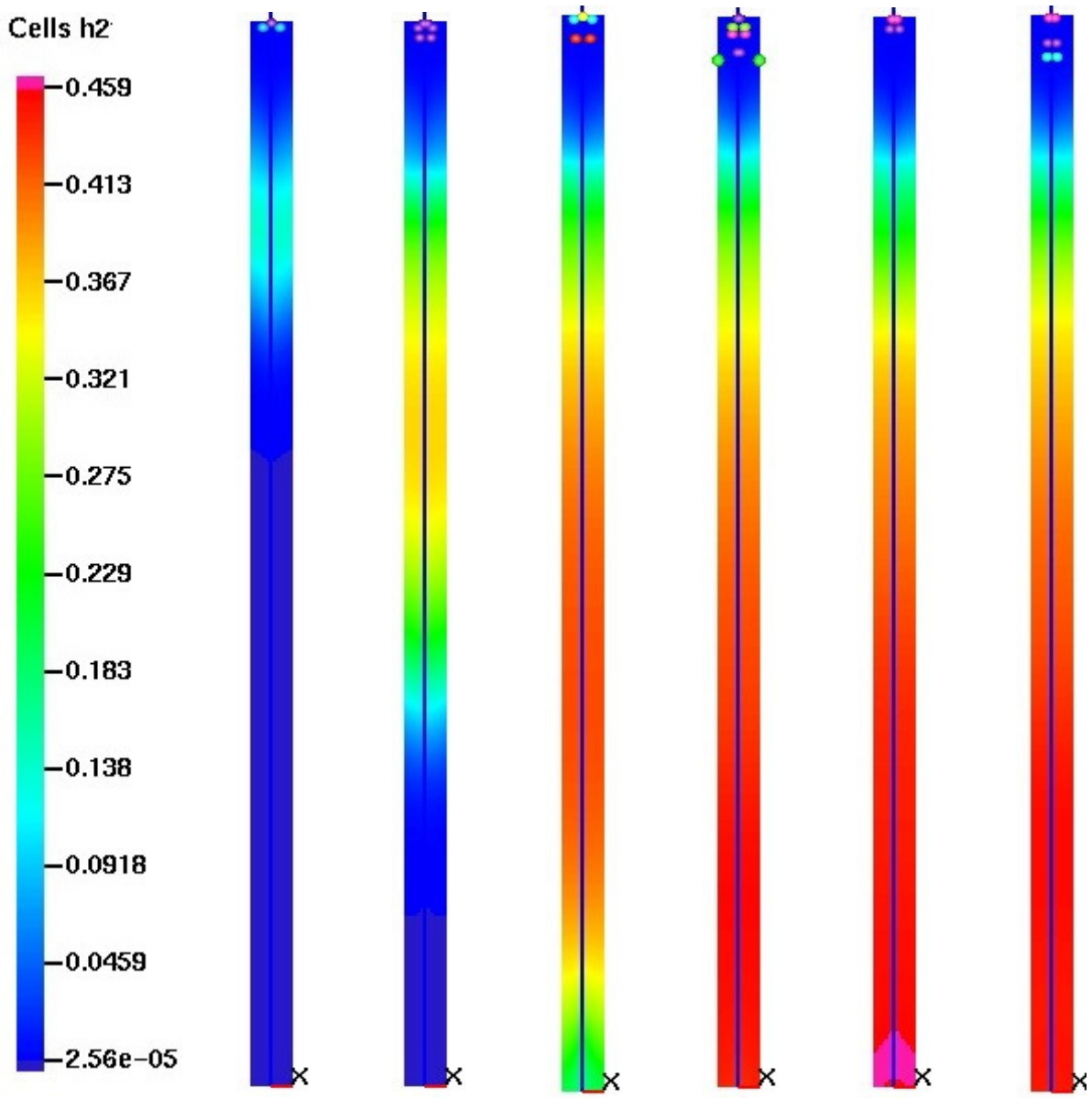

Figure 4.11. Hydrogen mole fraction distribution during the first 4 seconds of operation. Fuel mass flow rate is 0.132 g/s and the corresponding equivalence ratio is 0.25 at atmospheric pressure and 850 ºC. The distribution of hydrogen mole fraction is presented every 0.33 sec.

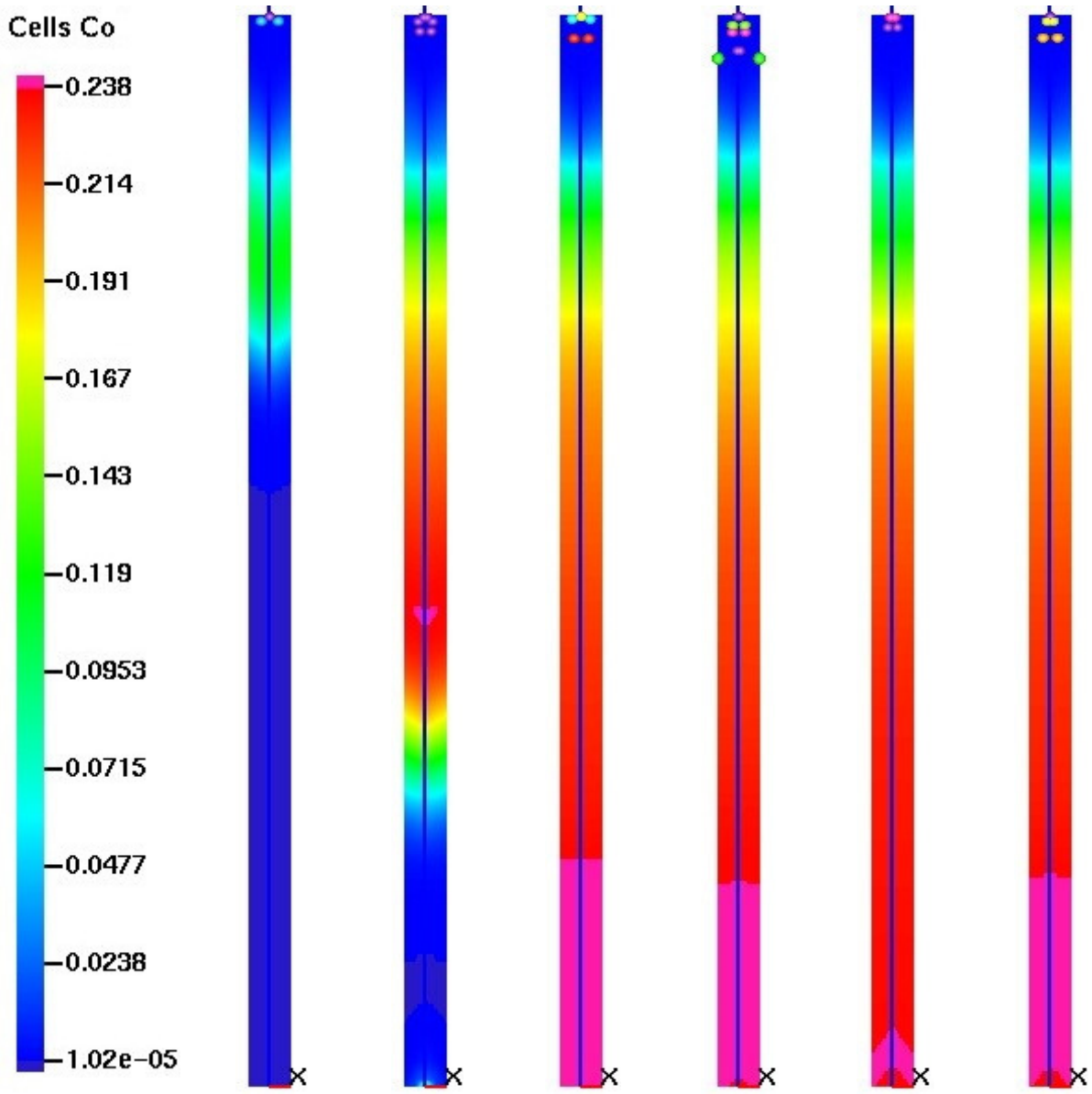

Figure 4.12. Carbon monoxide mole fraction distribution during the first 4 seconds of operation. Fuel mass flow rate is 0.132 g/s and the corresponding equivalence ratio is 0.25 at atmospheric pressure and 850 ºC. The distribution of carbon monoxide mole fraction is presented every 0.33 sec.

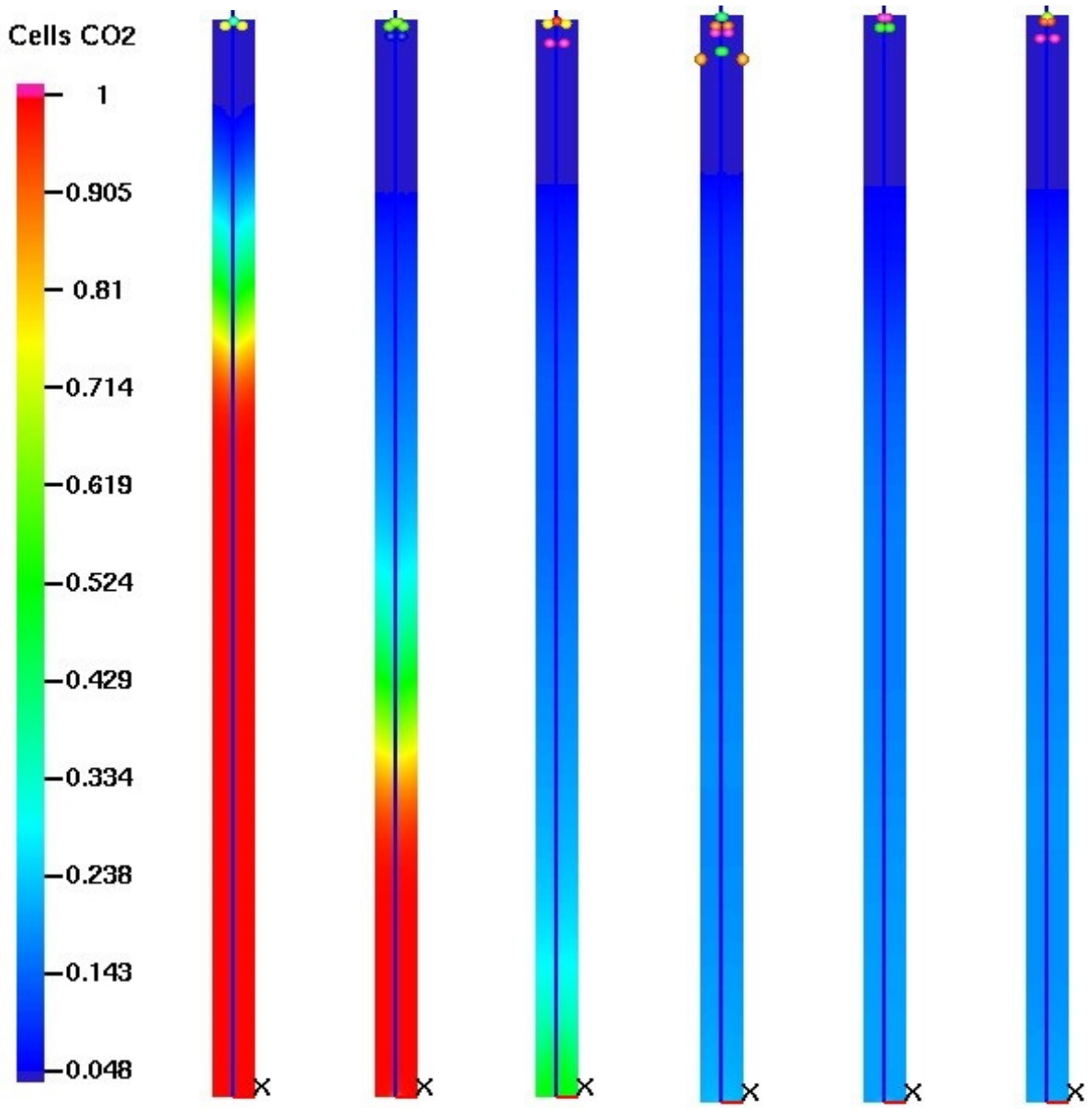

Figure 4.13. Carbon dioxide mole fraction distribution during the first 4 seconds of operation. Fuel mass flow rate is 0.132 g/s and the corresponding equivalence ratio is 0.25 at atmospheric pressure and 850 ºC. The distribution of carbon dioxide mole fraction is presented every 0.33 sec.

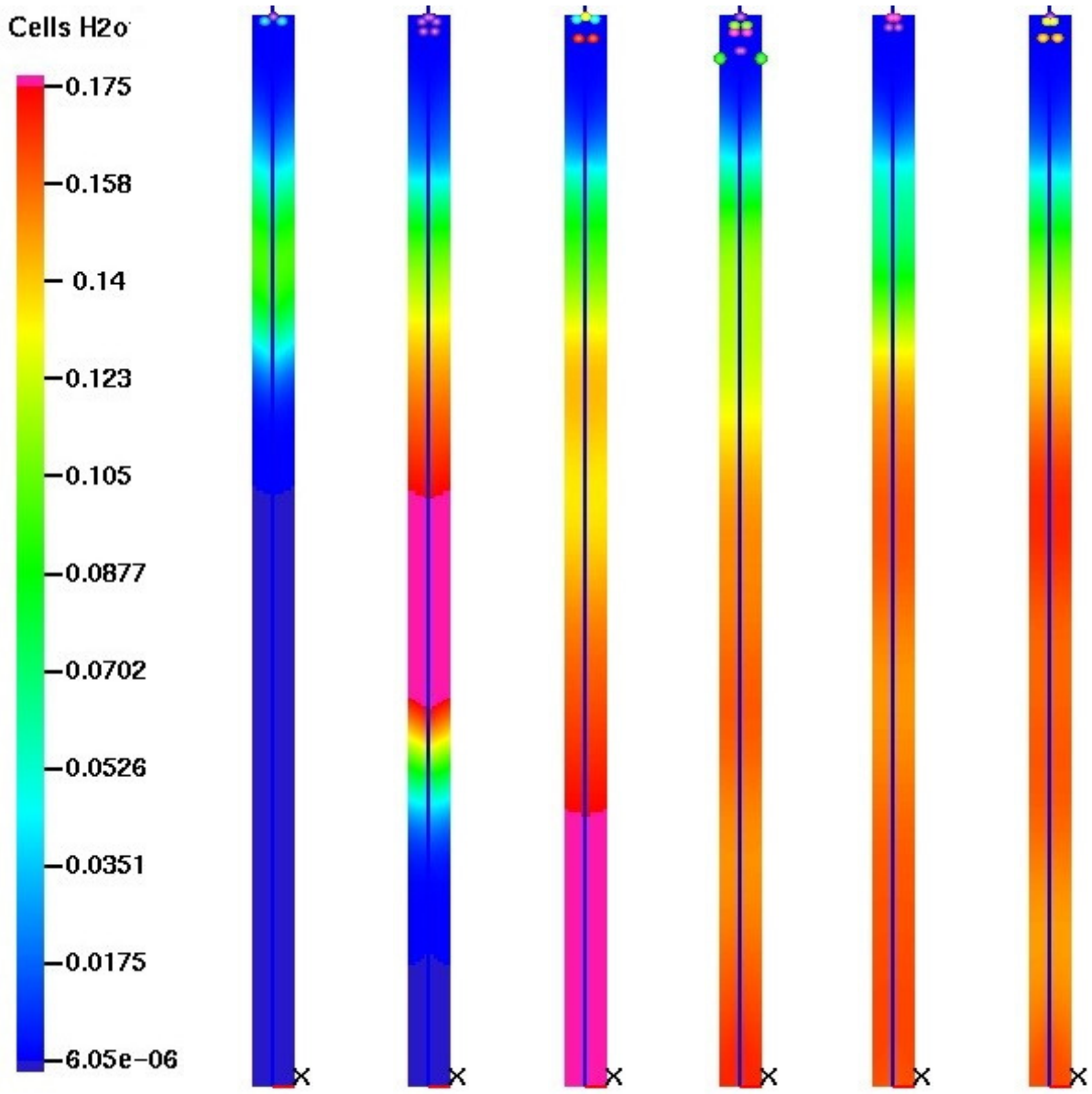

Figure 4.14. Water mole fraction distribution during the first 4 seconds of operation. Fuel mass flow rate is 0.132 g/s and the corresponding equivalence ratio is 0.25 at atmospheric pressure and 850 ºC. The distribution of water mole fraction is presented every 0.33 sec.

4.1.4 Validation of methanol gasification simulation

In this section, comparisons between the numerical results with the experimental data and equilibrium calculations are presented. Table 4.2 shows the dry mole fraction of gasification products at different equivalence ratios. The data include experimental data predictions using the present CFD code, and equilibrium calculations.

Table 4.2. Comparison of methanol gasification products mole fraction at different equivalence ratios. T=850ºC and P=0 psig

Products dry mole fraction	Equivalence ratio Φ=0.2			Equivalence ratio Φ=0.25			Equivalence ratio Φ=0.3		
	CFD (%)	EXP (%)	EQ (%)	CFD (%)	EXP (%)	EQ (%)	CFD (%)	EXP (%)	EQ (%)
H_2 (%)	55.31	--	59.3	54.79	56	59.8	51.05	--	54.9
CO (%)	28.22	--	30.1	28.78	33.9	30.5	25.84	--	28.1
CO_2 (%)	6.5	--	7.12	8.3	8.6	9.62	10.2	--	11.4

As can be seen, good agreement is obtained between the CFD simulation, experimental data, and equilibrium calculations. The current model can properly predict the syngas composition and temporal evolution of gasification products. Ideally gasification facilities work under high pressure to make it easier for downstream syngas processing. Table 4.3 shows the effect of operating pressure on the syngas composition. Both simulation and equilibrium calculations show no change in syngas yields at different operating pressures. It is apparent that the operating pressure does not have effects on the final products of methanol gasification.

Table 4.3. Comparison of methanol gasification products mole fraction at different operating condition. T=850ºC and Φ=0.25.

Products dry mole fraction	Operating pressure P=0 psig			Operating pressure P=100 psig			Operating pressure P=200 psig		
	CFD (%)	EXP (%)	EQ (%)	CFD (%)	EXP (%)	EQ (%)	CFD (%)	EXP (%)	EQ (%)
H_2 (%)	54.79	56	59.8	54.79	--	59.8	54.79	--	59.8
CO (%)	28.78	33.9	30.5	28.78	--	30.5	28.78	--	30.5
CO_2 (%)	8.3	8.6	9.62	8.3	--	9.62	8.3	--	9.62

4.2 Thermophysical Properties of Bio-oil Components

Before presenting the numerical results of bio-oil gasification, calculation of the thermophysical properties of bio-oil is presented. Bio-oil has a very complex composition. In this study, based on the literature, we assume that bio-oil consists of 10 major components as listed in Table 4.4.

Table 4.4. Mass fraction of the ten major bio-oil components [80]

Components	Formula	MW(g/mol)	Mass fraction
Water	H_2O	18.02	21.10
Hydroxyacetaldehyde	$C_2H_4O_2$	60.05	21.77
Acetic acid	$C_2H_4O_2$	60.05	9.48
Hydroxypropanone	$C_3H_6O_2$	74.08	15.06
Levoglucosan	$C_6H_{10}O_5$	162.14	17.27
Propionic acid	$C_3H_6O_2$	74.08	1.25
(5H)-furan-2-one	$C_4H_4O_2$	84.07	2.37
Isoeugenol	$C_{10}H_{12}O_2$	164.21	10.79
Phenol	C_6H_6O	94.11	0.37
Syringol	$C_8H_{10}O_3$	154.16	0.54

Using the Joback method, which is a group contribution method, the thermophysical properties of bio-oil major components including, enthalpy, latent heat, vapor pressure, critical temperature, and critical pressure can be calculated. The first step in finding these properties is to identify the molecular structure and chemical bonds of each major component, except water whose properties are available in the literatures.

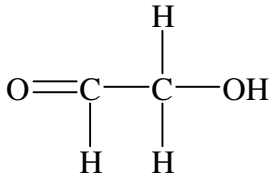

Hydroxyacetaldehyde

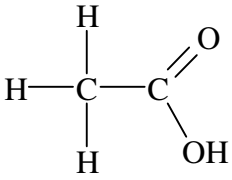

Acetic acid

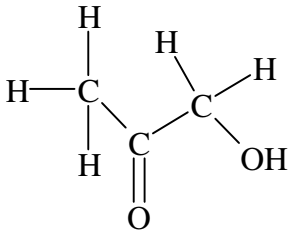

Hydroxypropanone

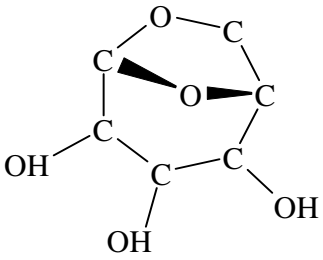

Levoglucosan

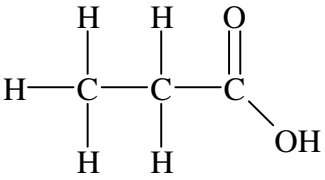

Propionic acid

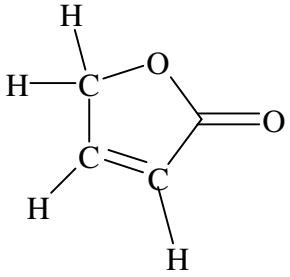

(5H)-furan-2-one

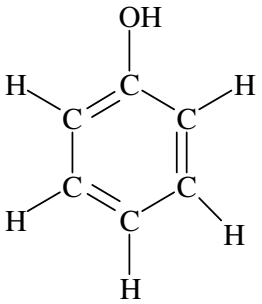

Phenol

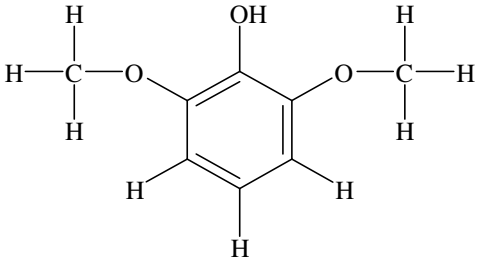

Syringol

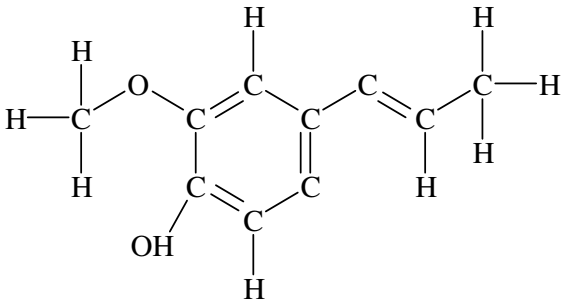

Isoeugenol

The corresponding chemical bonds for the above-mentioned components are listed in Table 4.5.

Table 4.5. Chemical bonds of each major component. R, P, and A denote a ring, phenol, and alcohol, respectively.

Bio-oil component	Contributing chemical bonds					
Hydroxyacetaldehyde	$-CH_2-$ (2)	OH-A (1)	O=C (1)	=CH- (1)	--	--
Acetic acid	$-CH_3$ (1)	>C=O (1)	OH-A(1)	>C= (1)	--	--
Hydroxypropanone	CH_3 (1)	>C=O (1)	OH-A(1)	$-CH_2-$ (2)	>C= (1)	--
Levoglucosan	OH-P(3)	-O-(2)	>CH-(5)	--	--	--
Propionic acid	CH_3 (1)	$-CH_2-$ (1)	>C=O (1)	OH-A(1)	>C= (1)	--
(5H)-furan-2-one	=CH-R(2)	$-CH_2-$R(1)	R>C=O (1)	O< R (1)	--	--
Isoeugenol	CH_3 (2)	OH-P(1)	-O- (1)	=CH-(2)	=CH-R (3)	=C< R(3)
Phenol	OH-P(1)	=CH-R (5)	--	--	--	--
Syringol	CH_3 (2)	-O- (2)	OH-P(1)	=CH-R(3)	=C<R (3)	--

By use of the Joback correlations (Eqs. (3.32)-(3.42)), the corresponding boiling temperature and critical values, including T_c and P_c, are obtained. Enthalpy will be obtained by integrating Eq. (3.39) from zero to the desired temperature.

Table 4.6. Properties of major components using Joback method.

Components	Formula	T_b (K)	T_c (K)	P_c (bar)
Water	H_2O	373	647	221
Hydroxyacetaldehyde	$C_2H_4O_2$	404	582	64.6
Acetic acid	$C_2H_4O_2$	391	588	57.3
Hydroxypropanone	$C_3H_6O_2$	418	595	54.8
Levoglucosan	$C_6H_{10}O_5$	578	733	57.0
Propionic acid	$C_3H_6O_2$	414	609	49.8
(5H)-furan-2-one	$C_4H_4O_2$	476	741	56.8
Isoeugenol	$C_{10}H_{12}O_2$	540	753	32.8
Phenol	C_6H_6O	460	702	61.4
Syringol	$C_8H_{10}O_3$	534	767	40.5

Other properties, including vapor pressure and latent heat, will be obtained using Eq. (3.43) and Eq. (3.48). It should be noted that, the Joback method is valid for a certain range of temperature

and it may give negative values for enthalpy at temperatures out of this range. In order to keep consistency in the enthalpy values, the ideal gas assumption (c_p constant) was adopted for high temperature range. The calculated vapor pressure, latent heat, and enthalpy are shown in Figure 4.15, Figure 4.16, and Figure 4.17, respectively.

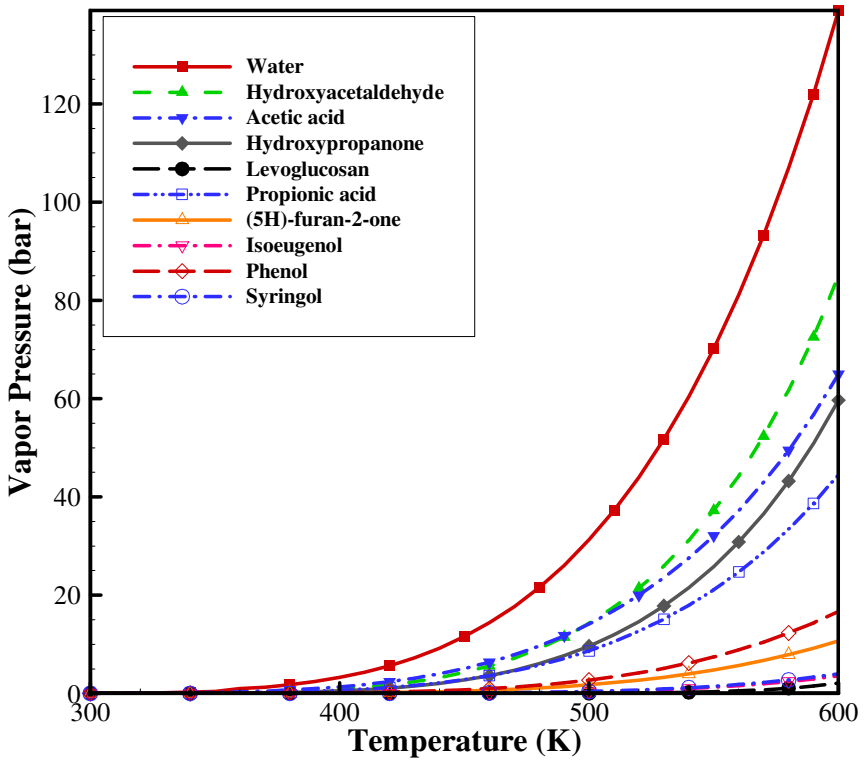

Figure 4.15. Vapor pressure of bio-oil major components at different temperatures

Among the major components of bio-oil, water has the highest vapor pressure and levoglucosan has the lowest. The results show that below 400 K, the vapor pressures of bio-oil components are almost zero, indicating the low volatility of these components. Higher vapor pressure means a faster vaporization rate. Besides vapor pressure, latent heat also plays an important role in the vaporization rate of a particular component.

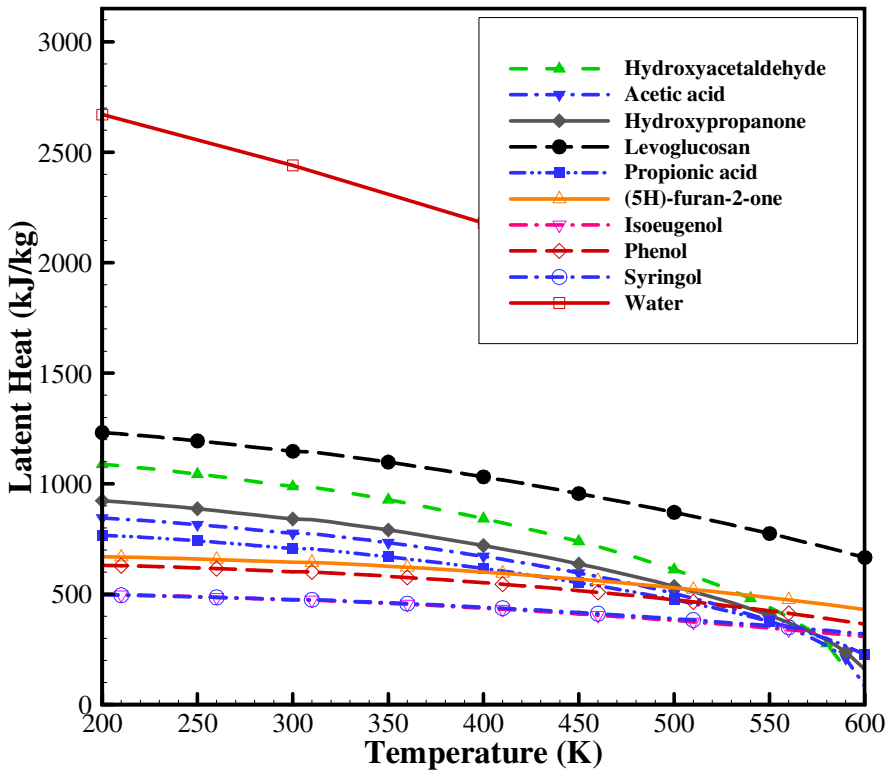

Figure 4.16. Latent heat of bio-oil major components at different temperatures

Compared to other components, water has the highest value of latent heat and the latent heat of other components are close to each other. It means that high amount of water can significantly impact the vaporization rate. The similar latent heat of other components indicates that these components may have similar behaviors in heat absorption. Figure 4.17 shows the enthalpy values for bio-oil major components. Enthalpy does not directly influence the vaporization rate but it will impact the chemical reactions and the resulting temperature. As stated earlier, the ideal gas assumption is adopted to calculate the enthalpy values at temperature ranges out of the Joback method formulation. By comparing the enthalpy of bio-oil components predicted by ideal gas calculation with enthalpy values of water, it is found that the ideal gas calculation for temperature ranges out of Joback method formulation is an acceptable assumption.

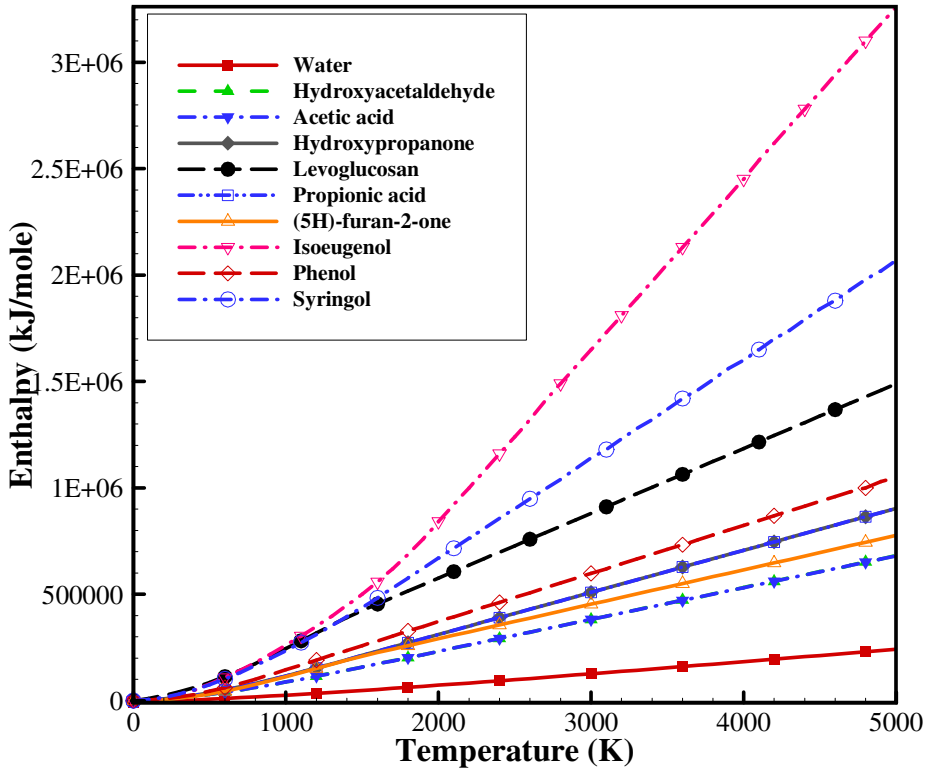

Figure 4.17. Enthalpy of bio-oil major components at different temperatures

4.3 Vaporization of Single Bio-oil Drop

Before presenting the simulation of bio-oil gasification, the vaporization of a single bio-oil drop is shown. The initial mass fraction of each major component is presented in Table 4.4. Figure 4.18 shows the mole fraction history of bio-oil major components. As can be seen, water is the first component vaporizes due to its relatively high vapor pressure. As the water content decreases, other components experience an increase in their mole fractions in the drop. Some components vaporize with delay and their mole fractions in the liquid phase show an increase as more volatile components leave the liquid earlier. The rapid reduction in their mole fractions in the liquid phase is observed after they reach their boiling points.

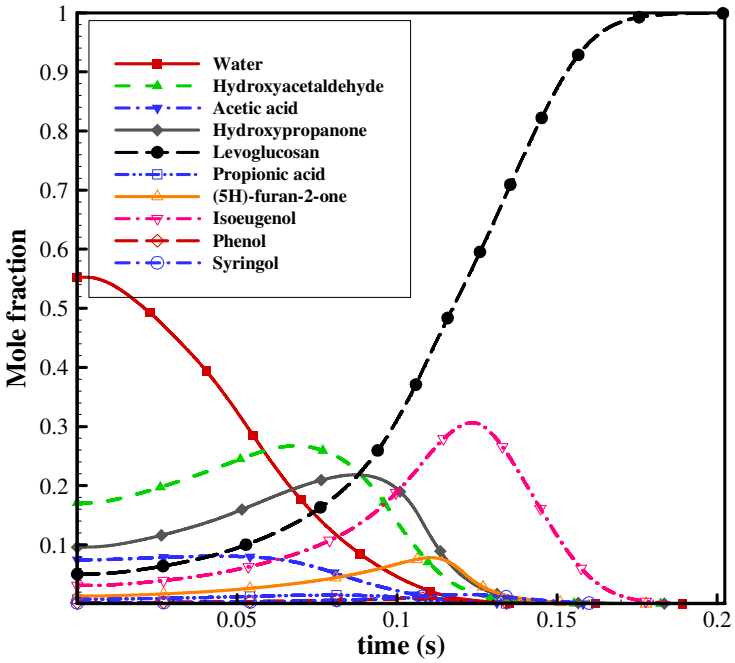

Figure 4.18. Mole fractions of bio-oil major components during drop vaporization

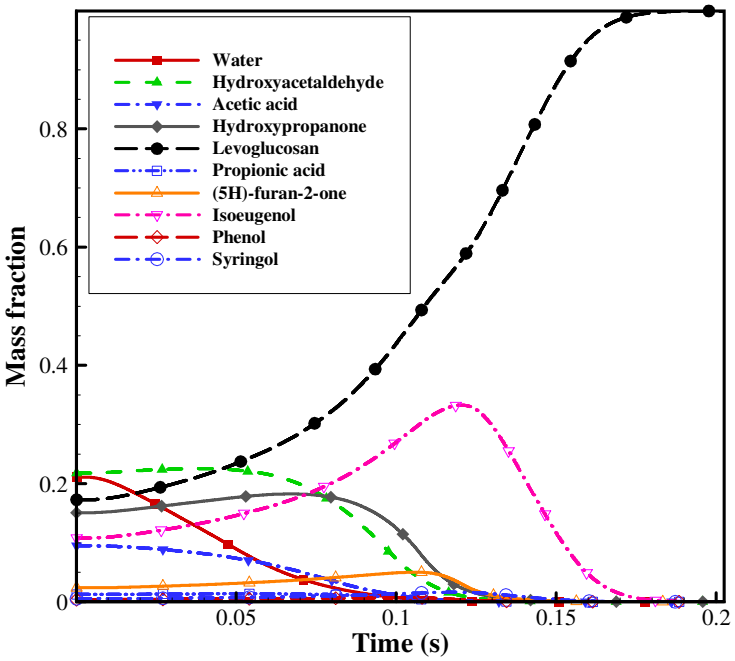

Figure 4.19. Mass fraction of Bio-oil major components during drop vaporization

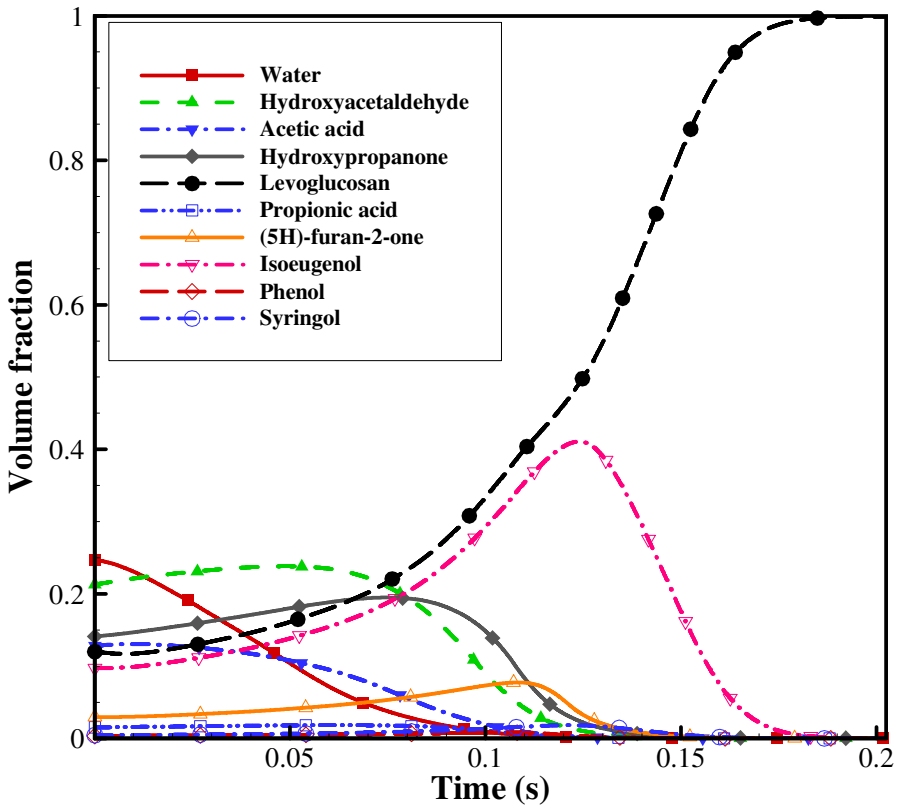

Figure 4.20. Volume fraction of Bio-oil major components during drop vaporization

As expected, levoglucosan is the last component remains in the bio-oil drop due to its relatively low vapor pressure and high boiling point. Same phenomena are observed for mass and volume fractions, as shown in Figure 4.19 and Figure 4.20. In general, vapor pressure and boiling temperature play significant roles in bio-oil vaporization.

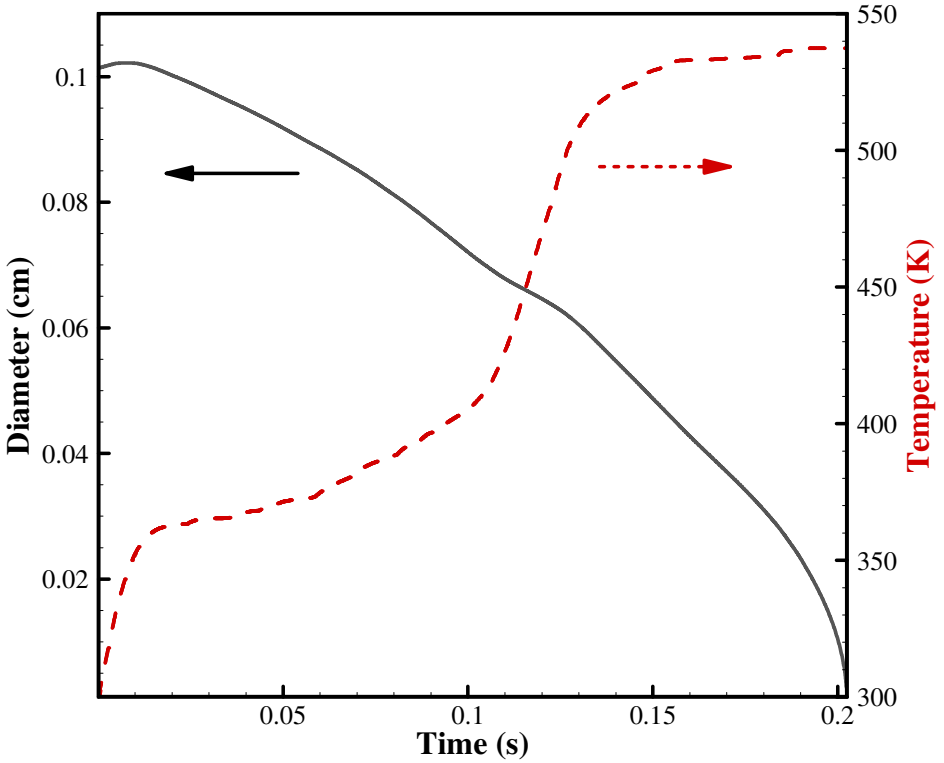

Figure 4.21. Bio-oil drop size and temperature histories during vaporization

The drop size and temperature histories are shown in Figure 4.21. At the beginning, the drop size grows until the most volatile component begins to vaporize. Before this time, the drop can be treated as a solid sphere that increases in size due to heat absorption. During this time, temperature increases and reaches the boiling point of the most volatile component, i.e., water. After vaporization starts, drop temperature continues to increase but its rate is not as fast. At the same time, the drop size decreases due to the drop components' migration from liquid phase to gas phase. A sharp raise of drop temperature is observed around t=0.11 s, and this is due to the fact that levoglucosan is the major component left in bio-oil drop and it takes time to reach its boiling point. After levoglucosan reaches its boiling point, it starts vaporizing and the drop temperature remains almost constant till the drop completely vaporizes.

4.4 Bio-oil Gasification

4.4.1 Modeling bio-oil gasification as a multi-component fuel

In this section, the mass fraction distribution of the bio-oil major components at 0.1 s after the start of injection and the final syngas composition of bio-oil gasification are presented. Figure 4.22 shows the vapor distribution of four of the bio-oil components at the early stage of the spray. The vapor distributions of other components are not shown as their mass fraction is relatively small and insignificant. As can be seen, the mass fraction of water is higher in regions close to the injector compared to other regions. As shown earlier, water vaporizes faster than the other components, and as the bio-oil drops move downstream, no water content is left in the drops.

On the other hand, the mass fractions of the other three components, including, levoglucosan, hydroxyacetaldehyde, and syringol, are relatively low in regions near the injector as they need more time to vaporize. The vaporization behaviors of the bio-oil components except water are very similar. Levoglucosan and syringol vapor pressure values are close to each other and their vaporization rates are approximately the same. Hydroxyacetaldehyde vaporizes faster than both levoglucosan and syringol, and its vapor mass fraction is higher in upper regions of the gasifier. Later in the spray vaporization process, less volatile components of bio-oil, such as levoglucosan and syringol, will produce more vapors in a region distant from the injector.

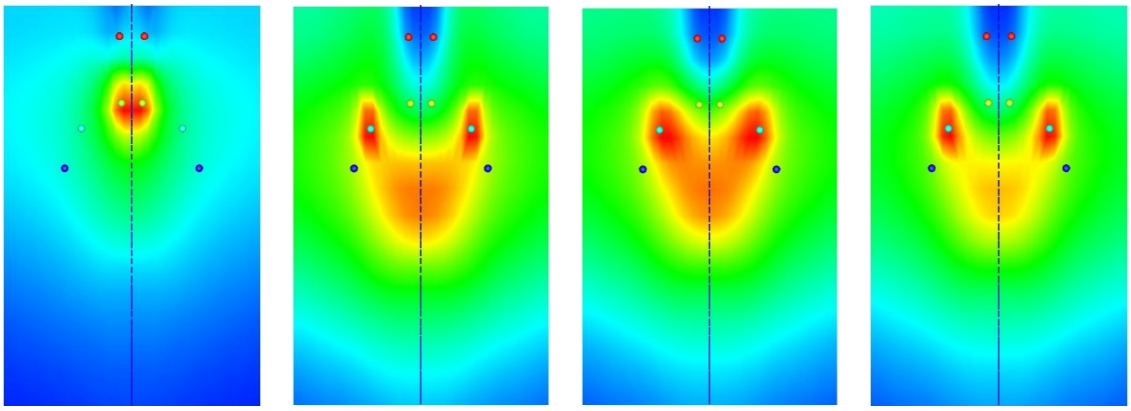

Water Levoglucosan Hydroxyacetaldehyde Syringol

Figure 4.22. Mass fractions of four major components of bio-oil after 0.1 s.

As bio-oil is injected into the gasifier, its major components vaporize at different rates. For instance, water leaves the bio-oil drop faster than other components, while heavy components, such as levoglucosan remains in the liquid drop longer. The original chemical reaction model only considers the gasification of single-component fuels. In this study, the chemical reaction model was modified to account for the gasification of multi-component fuels. The mass average approach was used as described in the following.

- Calculate the mass fractions of bio-oil vapor components.
- Calculate the total number of carbon, oxygen, and hydrogen of bio-oil components except water.
- Calculate the equilibrium values of bio-oil (as a single-component fuel) and products.
- Calculate the instantaneous values of bio-oil components based on the mass fraction distribution calculated in the first step.

To summarize, the modified chemical reactions model, considers bio-oil as a single-component fuel, calculates the equilibrium state values, and updates the remaining fuel based on its initial vapor mass fraction values.

The mole fractions of the products of bio-oil gasification are shown in Table 4.7. No proper experimental data are available to compare with the numerical results. Note that different types of bio-oil have different compositions, resulting in different syngas compositions. An arbitrary composition was chosen to test the multi-component vaporization model and the modified chemical reactions model. For this particular type of bio-oil, the majority of products are in the form of syngas (CO and H_2).

Table 4.7. Dry mole fractions of Bio-oil gasification products at atmospheric pressure. T=850ºC and Φ=0.25

Products dry mole fraction	CFD (%)
H_2 (%)	39.77
CO (%)	35.10
CO_2 (%)	15.51

4.4.2 Modeling bio-oil gasification using a surrogate

As stated in Chapter 2, bio-oil is the product of biomass fast pyrolysis and its composition varies with feedstock and operating conditions. For instance, bio-oil obtained from red oak can have more water than bio-oil obtained from palm. The present multi-component vaporization model and chemical reactions model are highly dependent on the bio-oil composition. The syngas produced from bio-oil gasification depends on the overall number of carbon, oxygen, and hydrogen of bio-oil. Based on the ultimate analysis, a surrogate component, $C_4H_{4.75}O_5$, is used to simulate the bio-oil gasification. Thermophysical properties were updated using the mass average calculation based on major components listed in Table 4.4. Figure 4.23 shows the spray and vapor of this bio-oil surrogate inside the gasifier for the first 0.1 second of its injection. The interval of the results shown in Figure 4.23 is every 0.06 sec from left to right.

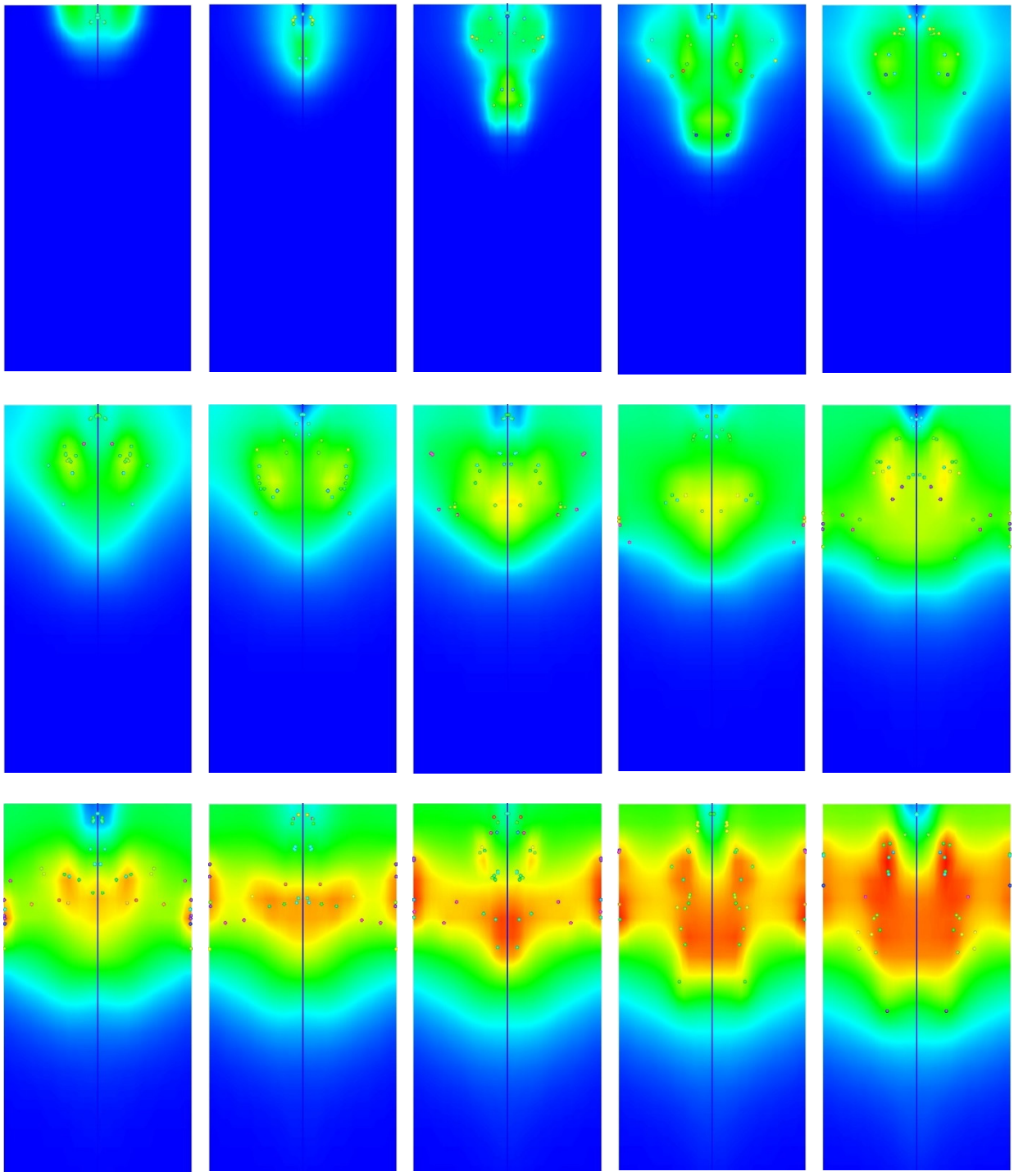

Figure 4.23. Spray and vapor distribution of bio-oil surrogate during the first 0.1 s of the injection. Fuel mass flow rate is fixed at 0.132 g/s with 25% theoretical air. Pressure and temperature are fixed at 0 psig and 850 ºC, respectively. The time interval between graphs is 6 ms. Only the top 7 cm of gasifier is illustrated in vertical direction.

As illustrated in Figure 4.23, bio-oil drops vaporize as they are injected and the fuel vapor occupies the gasifier and moves downstream as more bio-oil vaporizes. As more bio-oil is injected into the gasifier, more liquid bio-oil vaporizes. The mole fraction of bio-oil surrogate is higher in the regions close to wall and center. In the central region, the vaporization rate is higher because the injected oxygen helps atomize the bio-oil, improving its vaporization rate. On the other hand, the heated wall helps the bio-oil drops vaporize as they hit the wall. The bio-oil vapor distribution shows that a reasonably homogeneous mixture of fuel and oxygen can be achieved before the chemical reactions start.

With the present models for spray, vaporization and chemical reactions, the syngas evolution resulting from bio-oil gasification is obtained. Bio-oil mass flow rate is fixed at 0.132 g/s and the gasifier operates at atmospheric pressure and 850 ºC. Like methanol gasification, mole fractions of bio-oil and products for the first 4 seconds of simulation are shown in Figure 4.24 to Figure 4.28. As can be seen, the fuel vaporizes and mixes with oxygen, forming a reasonably homogeneous mixture. Chemical reactions start and convert the reactants to products downstream of the gasifier. Numerical simulation shows that carbon monoxide reaches its equilibrium state faster than hydrogen. The fuel rich condition allows the production of hydrogen and carbon monoxide in higher percentage.

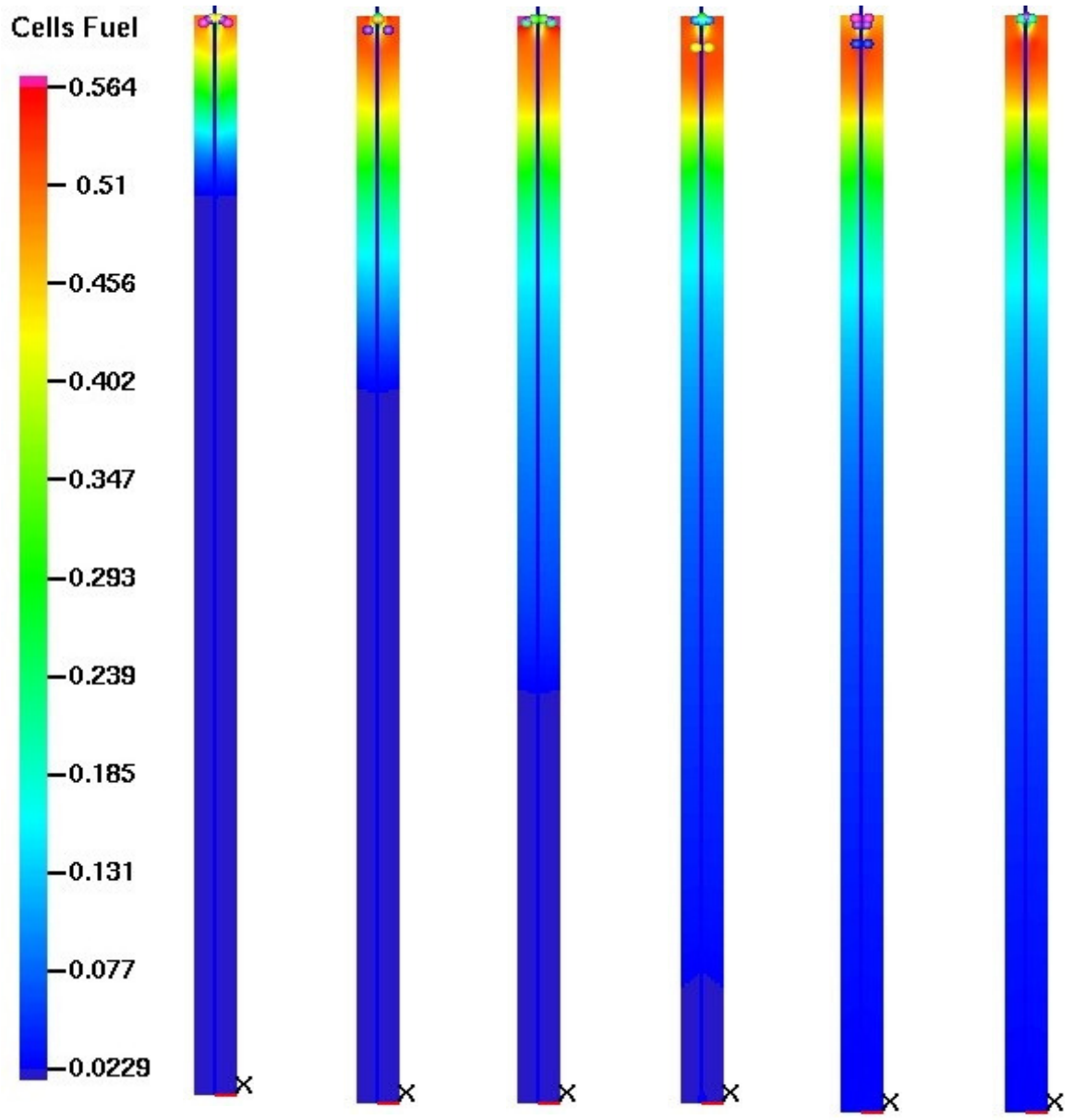

Figure 4.24. Bio-oil mole fraction distribution during the first 4 seconds of operation. Fuel mass flow rate is 0.132 g/s and the corresponding equivalence ratio is 0.25 at atmospheric pressure and 850 ºC. The distribution of bio-oil mole fraction is presented every 0.33 sec.

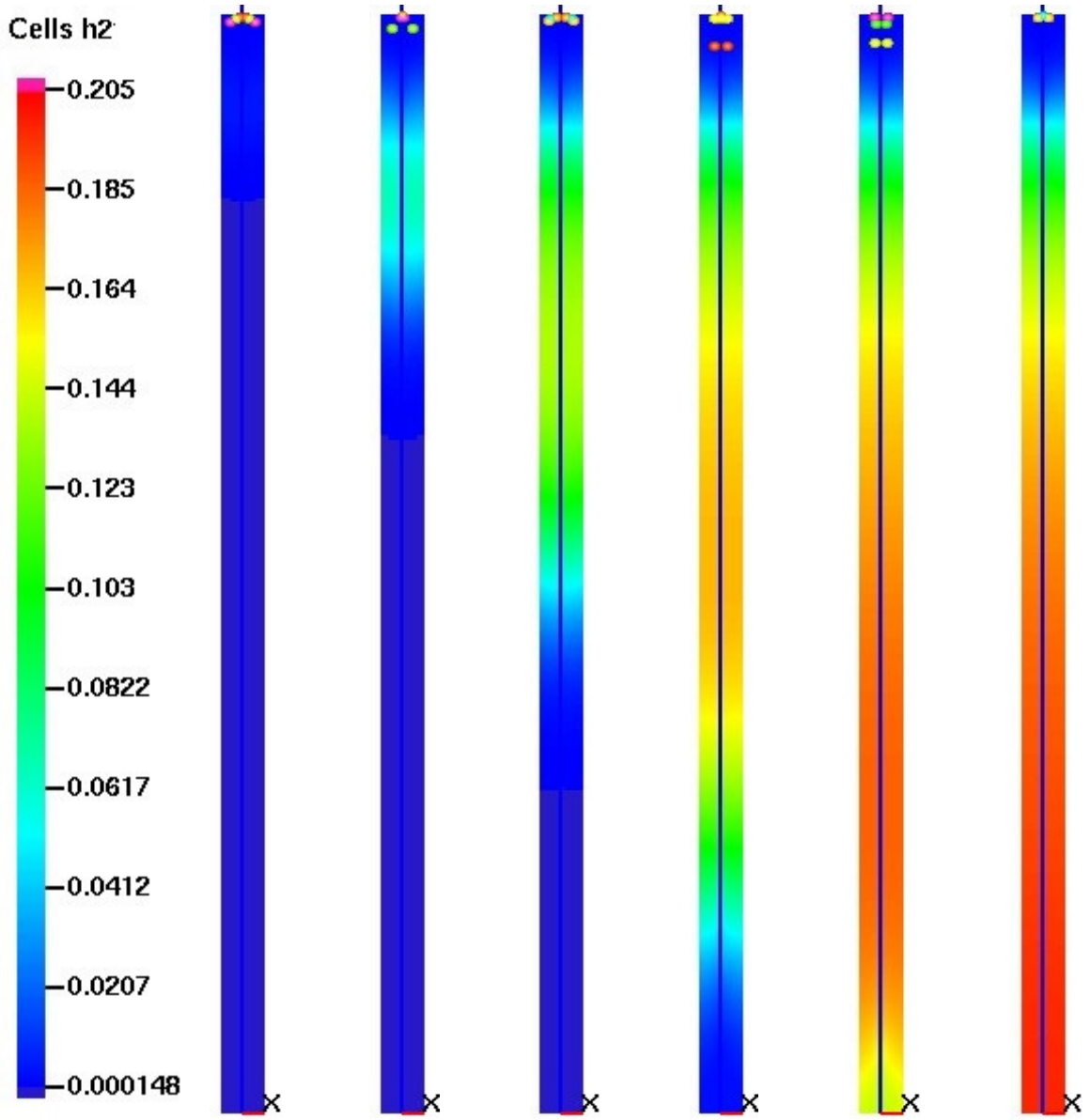

Figure 4.25. Hydrogen mole fraction distribution during the first 4 seconds of operation. Fuel mass flow rate is 0.132 g/s and the corresponding equivalence ratio is 0.25 at atmospheric pressure and 850 ºC. The distribution of hydrogen mole fraction is presented every 0.33 sec.

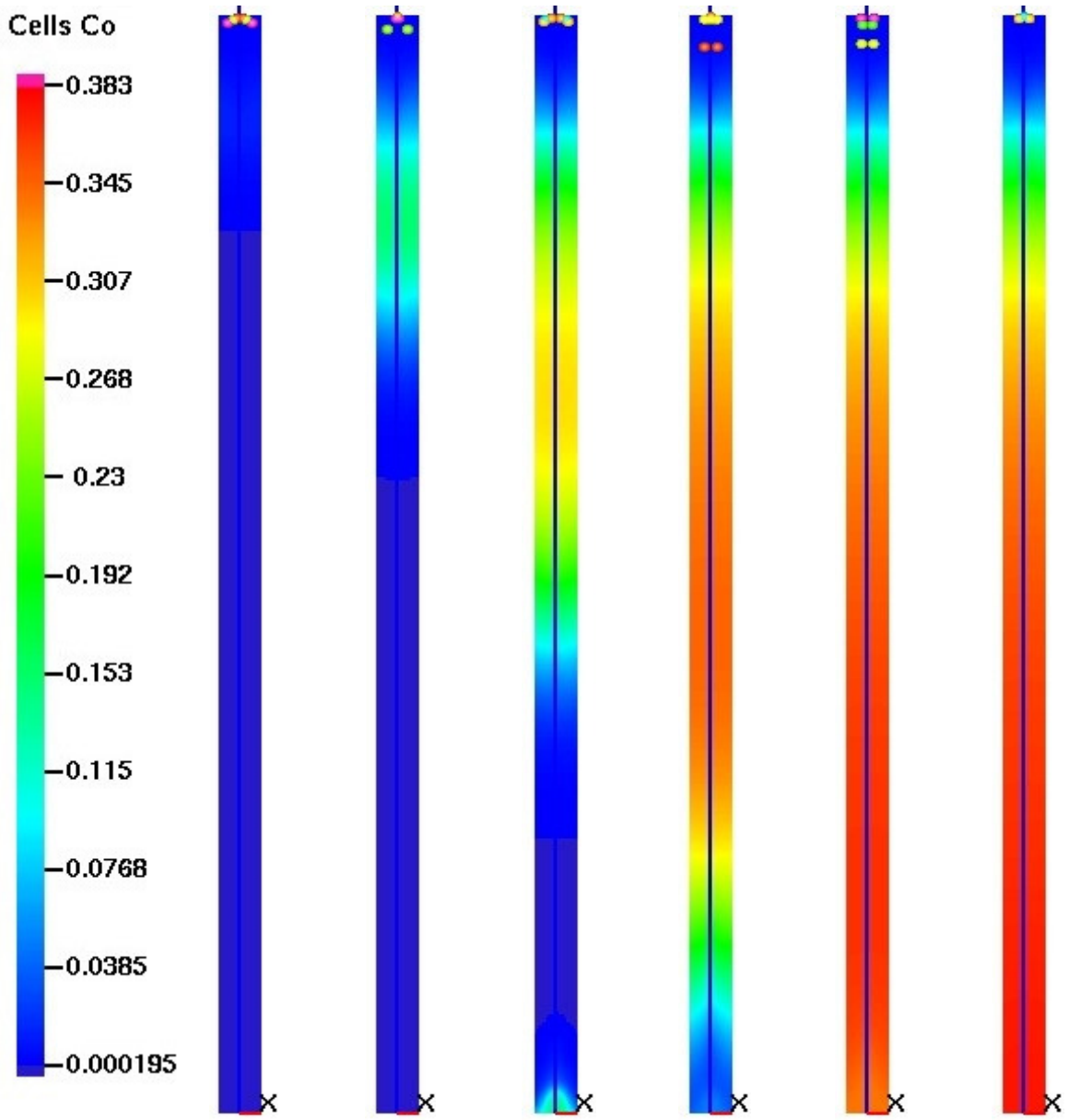

Figure 4.26. Carbon monoxide mole fraction distribution during the first 4 seconds of operation. Fuel mass flow rate is 0.132 g/s and the corresponding equivalence ratio is 0.25 at atmospheric pressure and 850 ºC. The distribution of carbon monoxide mole fraction is presented every 0.33 sec.

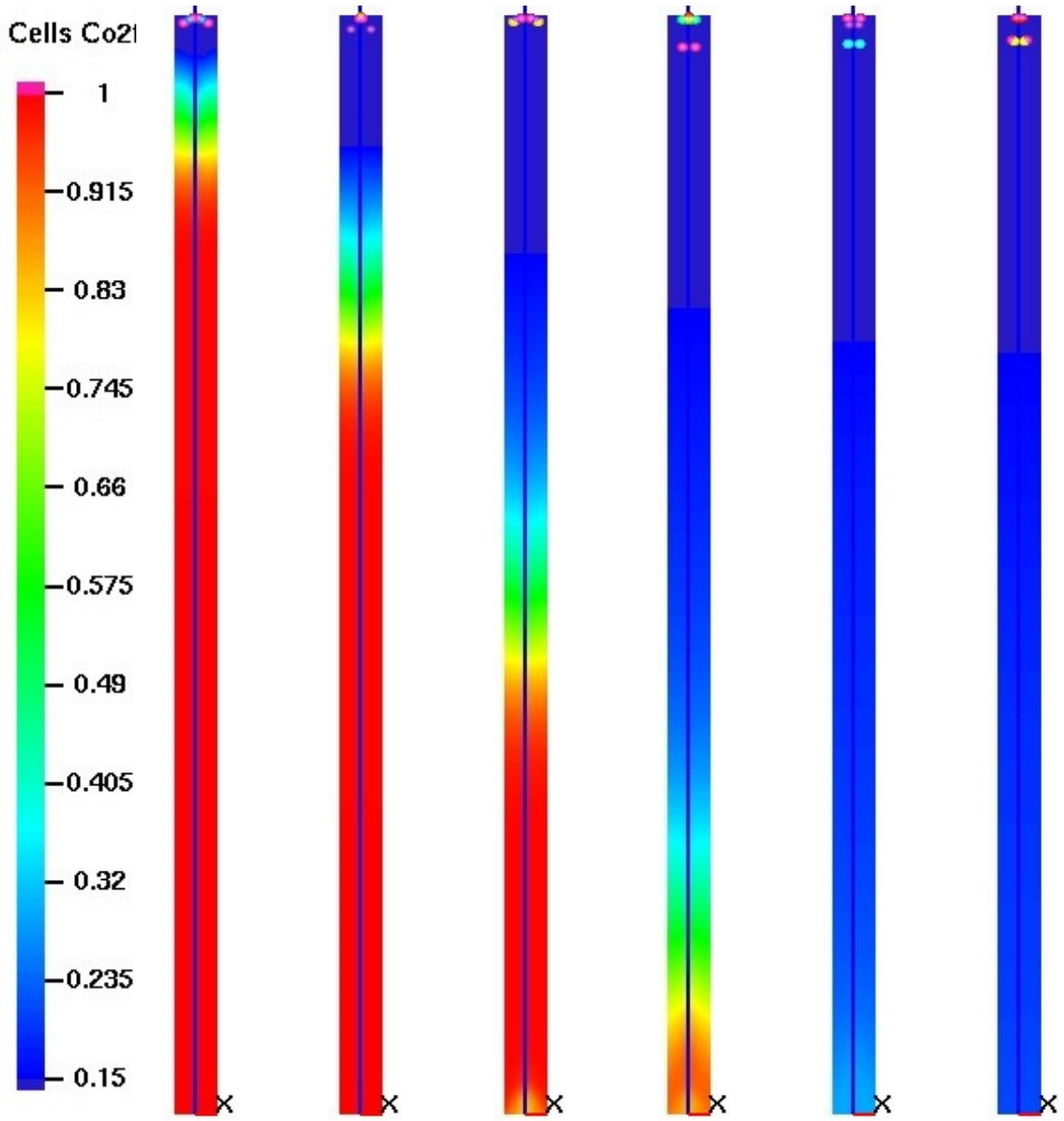

Figure 4.27. Carbon dioxide mole fraction distribution during the first 4 seconds of operation. Fuel mass flow rate is 0.132 g/s and the corresponding equivalence ratio is 0.25 at atmospheric pressure and 850 ºC. The distribution of carbon dioxide mole fraction is presented every 0.33 sec.

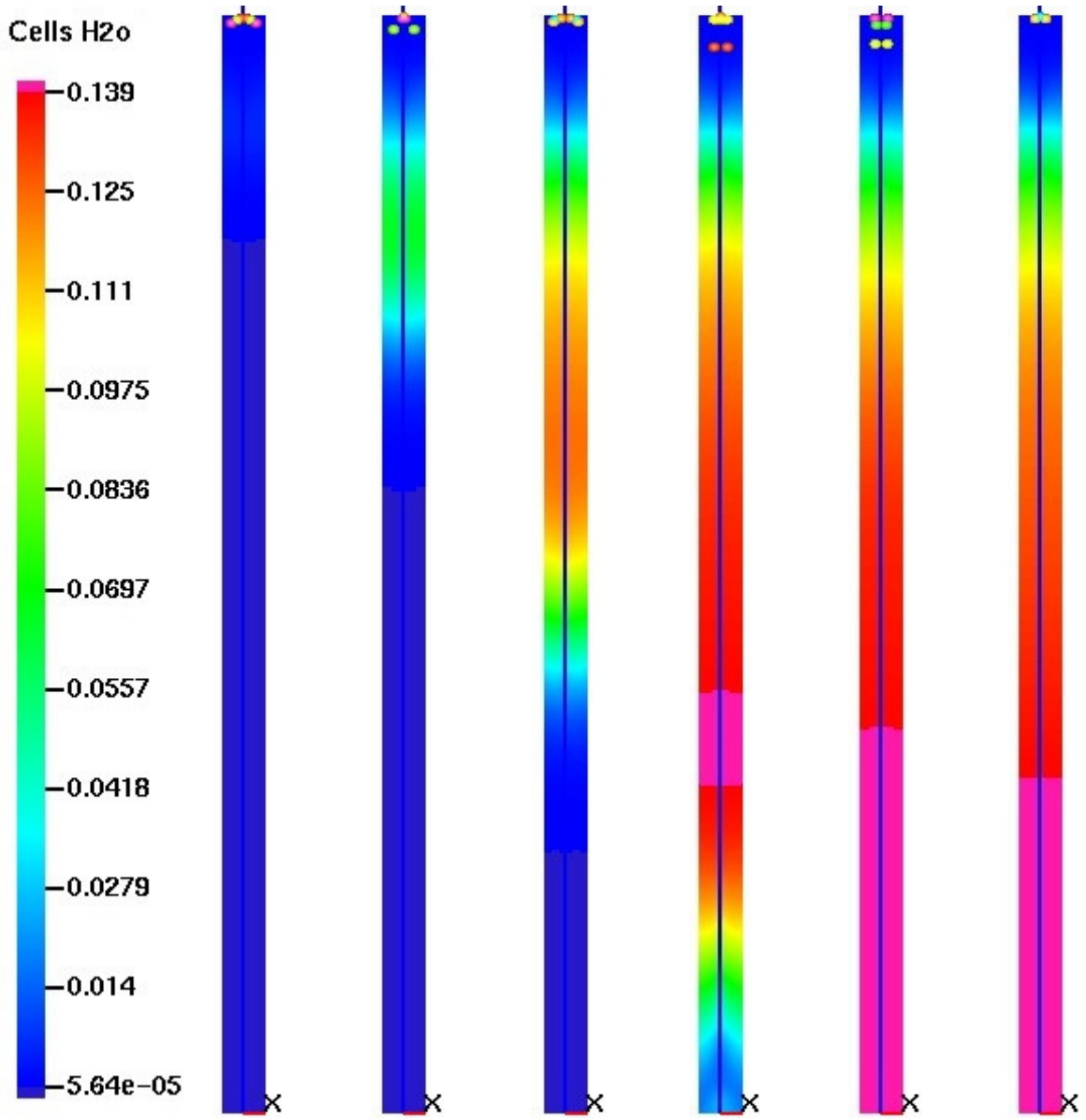

Figure 4.28. Water mole fraction distribution during the first 4 seconds of operation. Fuel mass flow rate is 0.132 g/s and the corresponding equivalence ratio is 0.25 at atmospheric pressure and 850 ºC. The distribution of water mole fraction is presented every 0.33 sec.

4.4.3 Comparison of bio-oil surrogate gasification results

In this section, comparisons between the numerical results and experimental data of bio-oil gasification are presented. Table 4.8 shows the dry mole fraction of gasification products at different operating pressures. The data include experimental data and predictions using the present CFD code. The good agreement between the CFD simulation and experimental data is reasonable, considering that the exact composition of bio-oil is unknown. As shown in Table 4.8, the gasification products do not show significant variations at different operating pressures. As stated earlier, high operating pressures help syngas downstream processes without changing the syngas composition.

Table 4.8. Comparison of bio-oil gasification products mole fraction at different operating condition. T=850ºC and Φ=0.25

Products mole fraction	Operating Pressure (psig)					Experimental data at psig=0
	0	100	200	362 (~ 25 bar)	725 (~ 50 bar)	
H_2 (%)	23.34	23.46	23.46	23.51	23.52	≈ 20
CO (%)	48.45	48.64	48.67	48.69	48.70	≈ 42
CO_2 (%)	22.79	22.55	22.52	22.50	22.49	≈ 25

Unlike methanol gasification in which hydrogen has the highest mole fraction value, bio-oil gasification results in more carbon monoxide. This is because that C/H (~ 1) in bio-oil is less than C/H (~ 0.25) in methanol. The presence of relatively high amount of carbon dioxide in bio-oil gasification products is caused by high oxygen content in bio-oil composition. It can be inferred that, for bio-oil with high oxygen, carbon dioxide can be significant in the gasification products. The difference between the numerical results and the experimental data is approximately 15% for CO, 16% for H_2 and 8% for CO_2. These differences can be improved if the more accurate composition of bio oil is provided.

The effects of equivalence ratio on the gasification products are studied and the results are presented in Table 4.9. As expected, the richer fuel mixture results in production of more syngas content in gasification products. At equivalence ratio of 0.2, CO and H_2 yields increase by 2.6% and 7.1%, compared to equivalence ratio of 0.25, and CO_2 production shows 11.5% reduction. Table 4.9 shows that CO_2 production is more sensitive to the equivalence ratio variations than CO and H_2. H_2 dependency on the equivalence ratio variations is almost three times more than CO. The numerical results of equivalence ratio of 0.3 shows that for a leaner fuel mixture, CO and H_2 production reduce by 3.6% and 7.3%, respectively, while CO_2 production augments by 13.69%. These results indicate CO_2 is more sensitive to the equivalence ratio variation.

Table 4.9. Comparison of bio-oil gasification products mole fraction at different equivalence ratio. T=850ºC and P=0 psig

Products mole fraction	Equivalence ratio		
	Φ=0.2	Φ=0.25	Φ=0.3
H_2 (%)	25.01	23.46	21.61
CO (%)	49.72	48.64	46.66
CO_2 (%)	20.17	22.55	25.91

4.5 Characteristics of Large Scale Gasifiers

The gasifier studied so far is designed to gasify 20 kg of bio-oil per day (i.e., ~ 0.132 g/s). The commercial facilities of bio-oil gasification are required to gasify high amount of bio-oil up to 1200 tons/day (i.e., ~ 7.92 kg/s). Therefore, new designs of gasifier are needed to meet the gasification of high amount of bio-oil. A gasifier should be designed in a way to provide a reasonably homogenous mixture of fuel and oxygen at a certain distance from the injectors. As stated earlier, a proper mixture of fuel and oxygen allows a complete chemical conversion to the

equilibrium state. The design, including the size of the injector and injection pressure, should be selected in a way to maximize the drops atomization and vaporization rate. Moreover, the reactor size, including the diameter and length must allow the complete conversion of bio-oil to syngas.

In this section, the vaporization of bio-oil and syngas production in a pilot-scale gasifier is studied. The pilot-scale gasifier is a cylinder with 30 cm in diameter and 300 cm in length. The injection pressure is fixed at 380 bar to inject 6 tons/day (i.e., ~ 65 g/s) of bio-oil. The injector diameter is 0.5 mm to enhance fuel atomization. Figure 4.29 shows the mole fraction of CO for the first 8 seconds of bio-oil gasification in the pilot-scale gasifier. As can be seen, bio-oil drops vaporize completely at approximately 100 cm from the injector. Syngas production starts from the regions close to wall where the temperature is high. As more fuel vaporizes and reacts with oxygen, the syngas yield increases and eventually occupies most of the gasifier. The results show that the present pilot-scale gasifier can properly meet the spray, vaporization, and chemical reactions required for higher gasification capacity up to 6 ton/day of bio-oil.

At even a larger scale, gasification of large amount of bio-oil can be obtained by using multiple injectors in a large gasifier. Based on the present results, a gasifier with 200 cm in diameter and 300 cm in length, which houses 20 injectors on top, can gasify bio-oil up to 120 ton/day. Using 10 separate gasifiers with the proposed geometry can help reach the goal of gasification of 1200 tons of bio-oil per day. This quantity of bio-oil corresponds to approximately 2000 ton/day of solid biomass that is used for fast pyrolysis.

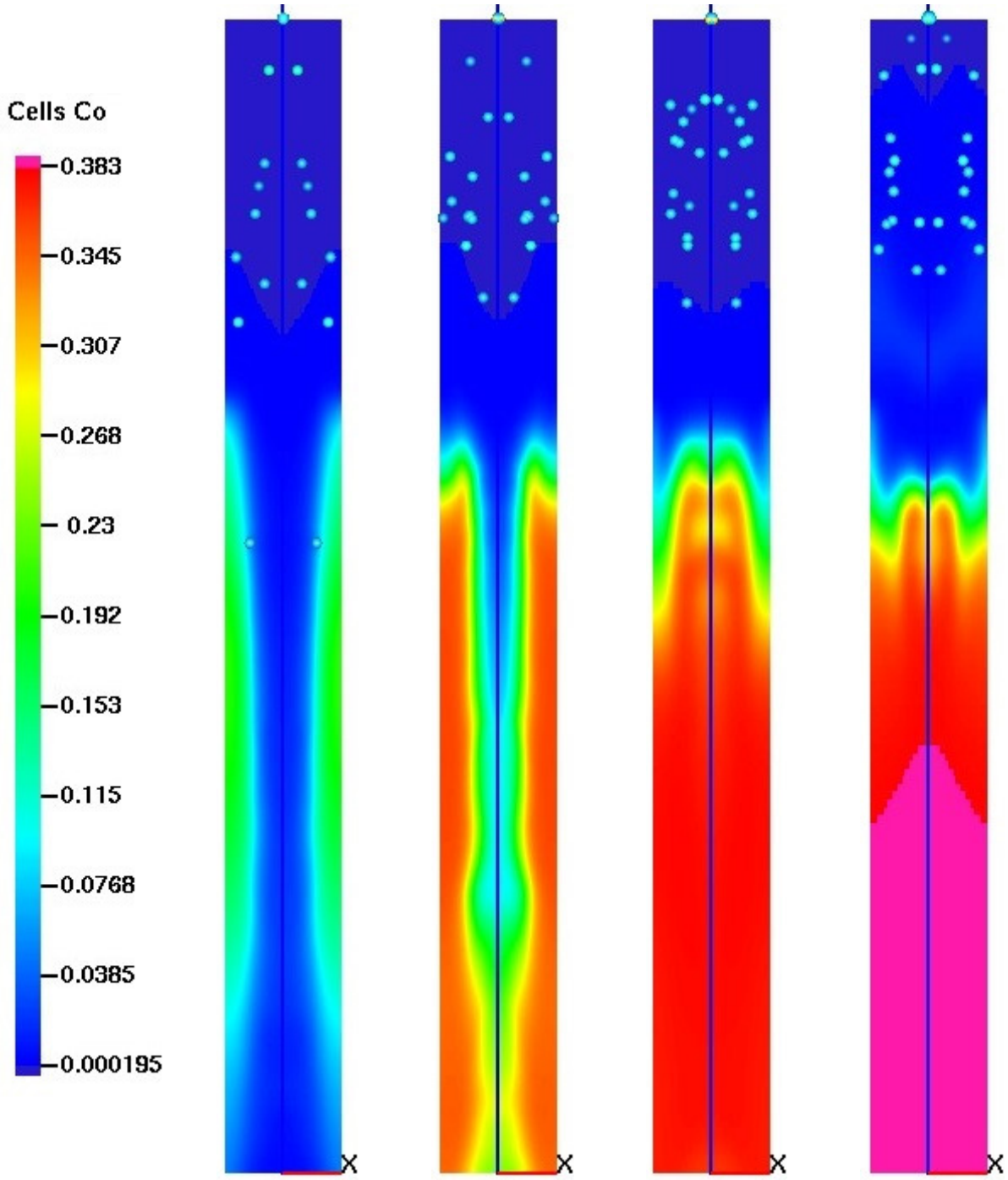

Figure 4.29. Carbon monoxide mole fraction distribution during the first 8 seconds of operation. Fuel mass flow rate is 64.37 g/s and the corresponding equivalence ratio is 0.25 at 50 bar and 850 ºC. The distribution of carbon monoxide mole fraction is presented every 2 sec.

CHAPTER 5. CONCLUSION

5.1 Summary

A comprehensive numerical model was developed to simulate the gasification of bio-oil at different operating conditions. KIVA-3V was used to solve the governing equations of fluid, heat, and mass transfer. The present model considers spray, vaporization, and chemical reactions during the gasification process. Bio-oil was considered as both single and multi-component fuel, consisting of ten various major components. The model can perfectly estimate the vaporization of bio-oil as a multi-component fuel. The Joback method was used to calculate the critical properties, e.g. critical pressure and temperature, latent heat, and enthalpy at different temperatures. Knowing the bio-oil major components' thermophysical properties, vaporization of single bio-oil drops was simulated and it was found that the heaviest component, levoglucosan, is the last component which leaves the liquid phase. Bio-oil gasification was simulated at different operating pressures and different equivalence ratios.

Thermodynamic equilibrium approach was used to evaluate chemical reactions. The numerical results of methanol and bio-oil gasification were validated using experimental data. It was found that the syngas yield is independent of the operating pressure but sensitive to equivalence ratio. It was also found that a fuel rich mixture results in high percentage of syngas while a lean condition produces more carbon dioxide and water. It was shown that syngas reaches the state of thermodynamic equilibrium gradually along the reactor. The model was applied to simulate bio-oil gasification at large reactors with bio-oil flow rate up to 6 ton/day. It was shown, a reactor with 30 cm in diameter and 300 cm in length and bio-oil fuel rate of 6 ton/day, the gasification products can reach their equilibrium states at the reactor outlet.

5.2 Future Work

Recommendations for future study is to develop a more comprehensive model that considers more equilibrium reactions to predict more species (e.g., methane) in final gasification products. A detailed kinetic model can be used to study the complex chemical reactions occurring in gasification process. As partial oxidation has been observed during gasification, developing a model that can predict this phenomenon can be useful. Simulations using a three-dimensional domain with multiple injectors can also provide useful insight to designing a high-performance gasifier.

REFERENCES

1. Basu P, (2010). Biomass gasification and pyrolysis: practical design and theory. Burlington, MA: Elsevier.
2. Kamarudin, S.K.; Shamsul, N.S.; Ghani, J.A.; Chia, S.K.; Liew, H.S.; Samsudin, A.S. Production of methanol from biomass waste via pyrolysis. Bioresource Technology. 2013, 129, 463-8.
3. Moghadam, R.A.; Yusup, S.; Azlina, W.; Nehzati, S.; Tavasoli, A. Investigation on syngas production via biomass conversion through the integration of pyrolysis and air‐steam gasification processes. Energy Conversion and Management. 2014, 87, 670-5.
4. Martinez, J.D.; Murillo, R.; Garcia, T.; Arauzo, I. Thermodynamic analysis for syngas production from volatiles released in waste tire pyrolysis. Energy Conversion and Management. 2014, 81, 338-53.
5. Nipattummakul, N.; Ahmed, I.I.; Gupta, A.K.; Kerdsuwan, S. Hydrogen and syngas yield from residual branches of oil palm tree using steam gasification. International Journal of Hydrogen Energy. 2011, 36, 3835-43.
6. Goransson, K.; Soderlind, U.; He, J.; Zhang, W. Review of syngas production via biomass DFBGs. Renewable and Sustainable Energy Reviews. 2011, 15, 482-92.
7. Bridgwater, A.V.; Peacocke, G.V.C. Fast pyrolysis processes for biomass. Renewable & Sustainable Energy Reviews. 2000, 4, 1–73.
8. Shafizadeh, F.; Furneaux, R.H.; Cochran, T.G.; Scholl, J.P.; Sakai, Y. Production of levoglucosan and glucose from pyrolysis of cellulosic materials. Journal of Applied Polymer Science. 1979, 23, 3525–39.

9. Chlup, Z.; Cerny, M.; Strachota, A.; Sucharda, Z.; Halasova, M.; Dlouhy, I. Influence of pyrolysis temperature on fracture response in SiOC based composites reinforced by basalt woven fabric. Journal of the European Ceramic Society. 2014, 34, 3389-98.
10. Yuan, H.; Lu, T.; Wang, Y.; Huang, H.; Chen, Y. Influence of pyrolysis temperature and holding time on properties of biochar derived from medicinal herb (radix isatidis) residue and its effect on soil CO_2 emission. Journal of Analytical and Applied Pyrolysis. 2014. In press.
11. Sandouk-Lincke, N.A.; Schwarzbauer, J.; Hartkopf-Fröder, C.; Volk, H.; Fuents, D.; Young, M.; Littke, R. The effect of different pyrolysis temperatures on organic microfossils, vitrain and amber-A comparative study between laser assisted- and Curie point-pyrolysis-gas chromatography/mass spectrometry. Journal of Analytical and Applied Pyrolysis. 2014, 107, 211-23.
12. Chen, Q.; Yang, R.; Zhao, B.; Li, Y.; Wang, S.; Wu, H.; Zhuo, Y.; Chen, C. Investigation of heat of biomass pyrolysis and secondary reactions by simultaneous thermogravimetry and differential scanning calorimetry. Fuel. 2014, 134, 467-76.
13. Larfeldt, J.; Leckner, B.; Melaaen, M.C. Modelling and measurements of heat transfer in charcoal from pyrolysis of large wood particles. Biomass and Bioenergy. 2000, 18, 507-514.
14. Onwudili, J.A.; Insura, N.; Williams, P.T. Composition of products from the pyrolysis of polyethylene and polystyrene in a closed batch reactor: Effects of temperature and residence time. Journal of Analytical and Applied Pyrolysis. 2009, 86, 293-303.

15. Katheklakis, I.E.; Shi-Lin, L.; Bartle, K.D.; Kandiyoti, R. Effect of freeboard residence time on the molecular mass distributions of fluidized bed pyrolysis tars. Fuel. 1990, 69, 172-6.

16. Tenegal, F.; Voicu I.; Armand, X.; Herlin-Boime, N.; Reynaud C. Residence time effect on fullerene yield in butadiene-based laser pyrolysis flame. Chemical Physics Letters. 2003, 379, 40-46.

17. Cuypers, F.; Helsen, L. Pyrolysis of chromated copper arsenate (CCA) treated wood waste at elevated pressure: Influence of particle size, heating rate, residence time, temperature and pressure. Journal of Analytical and Applied Pyrolysis. 2011, 92, 111-22.

18. Demiral, I.; Ayan, E.A. Pyrolysis of grape bagasse. Effect of pyrolysis conditions on the product yields and characterization of the liquid product. Bio- resource Technology. 2011, 102, 3946–51.

19. Ortega, J.V.; Renehan, A.M.; Liberatore, M.W.; Herring, A.M. Physical and chemical characteristics of aging pyrolysis oils produced from hard wood and softwood feedstocks. Journal of Analytical and Applied Pyrolysis. 2011, 91, 190–8.

20. Cao, J.; Xiao, X.; Zhang, S.; Zhao, X.; Sato, K.; Ogawa, Y.; Wei, X.Y.; Takarada, T. Preparation and characterization of bio-oils from internally circulating fluidized-bed pyrolysis of municipal, livestock, and wood waste. Bioresource Technology. 2011, 102, 2009–15.

21. Gercel, H.F. Bio-oil production from Onopordum acanthium L. by slow pyrolysis. Journal of Analytical and Applied Pyrolysis. 2011, 92, 233–8.

22. Onal, E.P.; Uzun, B.B.; Putun, A.E. Steam pyrolysis of an industrial waste for bio- oil production. Fuel Processing Technology. 2011, 92, 879–85.

23. Amutio, M.; Lopez, G.; Artetxe, M.; Elordi, G.; Olazar, M.; Bilbao J. Influence of temperature on biomass pyrolysis in a conical spouted bed reactor. Resources, Conservation and Recycling. 2012, 59, 23–31.

24. Thangalazhy-Gopakumar, S.; Adhikari, S.; Ravidran, H.; Gupta, R.B.; Fasina, O.; Tu, M.; Fernando, S.D. Physical properties of bio-oil produced at various temperature from pinewood using an auger reactor. Bioresource Technology. 2010, 101, 8389–95.

25. Heo, H.S.; Park, H.J.; Park, Y.K.; Ryu, C.; Suh, D.J.; Suh, Y.W.; Yim, J.H.; Kim, S.S. Bio-oil production from fast pyrolysis of waste furniture saw dust in a fluidized bed. Bioresource Technology. 2010, 101, 91–6.

26. Heo, H.S.; Park, H.J.; Dong, J.I.; Park, S.H.; Kim, S.; Suh, D.J.; Suh, Y.W.; Kim, S.S; Park, Y.K. Fast pyrolysis of rice husks under different reaction conditions. Journal of Industrial and Engineering Chemistry. 2010, 16, 27–31.

27. Islam, M.R.; Parveen, M.; Haniu, H. Properties of sugarcane waste-derived bio-oils obtained by fixed-bed fire-tube heating pyrolysis. Bioresource Technology. 2010, 101, 4162–8.

28. Mullen, C.A.; Boateng, A.A.; Goldberg, N.M.; Lima, I.M.; Laird, D.A.; Hicks, K.B. Bio-oil and bio-char production from corncobs and stover by fast pyrolysis. Biomass and Bioenergy. 2010, 34, 67–74.

29. Ertas, M.; Alma, M.H. Pyrolysis of laurel (Laurus nobilis L.) extraction residues in a fixed-bed reactor: characterization of bio-oil and bio-char, Journal of Analytical and Applied Pyrolysis. 2010, 88, 22–29.

30. Zhang, H.; Xiao, R.; Huang, H.; Xiao, G. Comparison of non-catalytic and catalytic fast pyrolysis of corncob in a fluidized bed reactor. Bioresource Technology. 2009, 100, 1428-34.

31. Asadullah, M.; Rahman, M.A; Ali M.M.; Motin, M.A.; Sultan, M.B.; Alam, M.R.; Rahman M.S. Jute stick pyrolysis for bio-oil production in fluidized bed reactor. Bioresource Technology. 2008, 99, 44–50.

32. Ozbay, N.; Apaydin-Varol, E.; Uzun, B.B.; Putun, A.E. Characterization of bio-oil obtained from fruit pulp pyrolysis. Energy. 2008, 33, 1233-40.

33. Lede, J.; Broust, F.; Ndiaye, F.T.; Ferrer, M. Properties of bio-oils produced by biomass fast pyrolysis in a cyclone reactor. Fuel. 2007, 86, 1800-10.

34. Xiong, Q.; Aramideh, S.; Passalacqua, A.; Kong, S.-C. BIOTC: An Open-Source CFD Code for Simulating Biomass Fast Pyrolysis, Computer Physics Communications. 2014, 185, 1739-46.

35. Xiong, Q.; Aramideh, S.; Kong, S.-C. Modeling effects of operating conditions on biomass fast pyrolysis in bubbling fluidized bed reactors, Energy & Fuels. 2013, 27, 5948-56.

36. Bridgewater, A.V.; Czernik, S.; Piskorz, J. Progress in thermochemical biomass conversion. Oxford: Blackwell Science. 2001.

37. Demirbas, A. Effect of Temperature on Pyrolysis Products from Biomass. Energy Sources. Part A 2010, 29, 329-36.

38. Cunha, J.A.; Pereira, M.M.; Valente, L.M.M.; de la Piscina, P.R.;, Homs, N.; Santos, M.R.L. Waste biomass to liquids: low temperature conversion of sugarcane bagasse to bio-oil. The effect of combined hydrolysis treatments. Biomass and Bioenergy. 2011, 35, 2106–16.

39. Das, P.; Ganesh, A.; Wangikar, P. Influence of pretreatment for deashing of sugarcane bagasse on pyrolysis products. Biomass and Bioenergy. 2004, 27, 445-457.

40. Kumar, P.; Barrett, D.M.; Delwiche, M.J.; Stroeve, P. Methods for pretreatment of lingo cellulosic biomass for efficient hydrolysis and biofuel production. Industrial & Engineering Chemistry Research. 2009, 48, 3713-29.

41. Bridgwater, A.V. Biomass fast pyrolysis. Thermal Sciences. 2004, 8, 21–49.

42. Czernik, S.; Bridgwater, A.V. Overview of applications of biomass fast pyrolysis oil. Energy and Fuels. 2004, 18, 590–8.

43. Islam, M.R.; Tushar, M.S.H.K.; Haniu, H. Production of liquids fuels and chemicals from pyrolysis of Bangladeshi bicycle/rickshaw tire wastes. Journal of Analytical and Applied Pyrolysis. 2008, 82, 96–109.

44. Wildschut, J. (2009). Pyrolysis Oil Upgrading to Transportation Fuels by Catalytic Hydrotreatment, thesis, University of Groningen.

45. Zhang, L.; Kong, S.C. Multicomponent vaporization modeling of bio-oil and its mixture with other fuels. Fuel. 2012, 9, 471-80.

46. Sipila, K.; Kuoppala, E.; Fagernas, L.; Oasmaa, A. Characterization of Biomass based Flash Pyrolysis Oils. Biomass and Bioenergy. 1998, 14, 103-113.

47. Hu, X.; Li, C.; Xu, Y.; Wang, Q.; Zhu, X. On the Thermal Oxidation Stability of Pyrolysis Biomass Oil. International Journal of Renewable Energy Technology. 2011, 2, 155-168.

48. Shihadeh, A.; Hochgreb, S. Diesel engine combustion of biomass pyrolysis oils, Energy and Fuels. 2000, 14, 260–74.

49. Zhang, L.; Kong, S.C. Vaporization modeling of petroleum-biofuel drops using a hybrid multicomponent approach. Combust Flame. 2010, 157, 2165–74.

50. Ra, Y.; Reitz R.D. A vaporization model for discrete multicomponent fuel sprays. International Journal of Multiphase Flow. 2009, 35, 101-12.
51. Huynh, C. V.; Kong, S.-C. Performance Characteristics of a Pilot-Scale Biomass Gasifier Using Oxygen-Enriched Air and Steam, Fuel. 2013, 103, 987–96.
52. Huynh, C. V.; Kong, S.-C. Combustion and NOx Emissions of Biomass-Derived Syngas under Various Gasification Conditions Utilizing Oxygen-Enriched-Air and Steam, Fuel. 2013, 107, 455–64.
53. The Encyclopaedia Britannica: A Dictionary of Arts, Sciences, Literature and General Information, Volumes 11-12, Hugh Chrisholm.
54. Latifi, M. Gasification of Bio-oil to Syngas in Fluidized Bed Reactors. Thesis, Western University, London, Ontario 2012.
55. Xue, Q.; Fox, R.O. Multi-fluid CFD modeling of biomass gasification in polydisperse fluidized-bed gasifiers. Powder Technology. 2014, 265, 23-34.
56. Blasi, C.D. Combustion and gasification rates of lignocellulosic chars. Progress in Energy and Combustion Science. 2009, 35, 121-140.
57. Petersen, L.; Werther, J. Experimental investigation and modeling of gasification of sewage sludge in the circulating fluidized bed. Chemical Engineering and Processing. 2005, 44, 717-736.
58. Higman, C.; Burgt, M. (2008) Gasification. Burlington, MA: Elsevier.
59. Gao, N.; Li, A.; Quan, C.; Gao, F. Hydrogen-rich gas production from biomass steam gasification in an updraft fixed-bed gasifier combined with porous ceramic reformer. International Journal of Hydrogen Energy. 2008, 33, 5430-38.

60. Hanaoka, T.; Hiasa, S.; Edashige, Y. Syngas production by CO_2/O_2 gasification of aquatic biomass. Fuel processing Technology. 2013, 116, 9-15.

61. Guo, H.; Peng, F.; Zhang, H.; Xiong, L.; Li, S.; Wang, C.; Wang, B; Chen, X.; Chen, Y. Production of hydrogen rich bio-oil derived syngas from co-gasification of bio-oil and waste engine oil as feedstock for lower alcohols synthesis in two-stage bed reactor. Interntional Journal of Hydrogen Energy. 2014, 39, 9200-11.

62. Yang, W.; Ponzio, A.; Lucas, C.; Blasiak, W. Performance analysis of a fixed-bed biomass gasifier using high-temperature air. Fuel Process Technol. 2006, 87, 235–45.

63. Di Blasi, C. Modeling wood gasification in a countercurrent fixed-bed reactor. AIChE Journal. 2004, 50, 2306–19.

64. Wurzenberger, J.C.; Wallner, S.; Raupenstrauch, H.; Khinast, J.G. Thermal conversion of biomass: comprehensive reactor and particle modelling. AIChE Journal. 2002, 48, 2398–41.

65. Umeki, K.; Namioka, T.; Yoshikawa, K. Analysis of an updraft biomass gasifier with high temperature steam using a numerical model. Applied Energy. 2012, 90, 38-45.

66. Stiesch, G.; (2004). Modeling Engine Spray and Combustion processes. Springer.

67. Reitz, R.D.; Bracco, F.V. Mechanisms of Breakup of Round Liquid Jets. Book Chapter the Encyclopedia of Fluid Mechanics, N. Cheremisnoff, Ed., Gulf Publishing, Houston, Texas, Vol. 3, Chapter 10, pp. 233-249, 1986.

68. Kuensberg, S.C.; Kong, S.C.; Reitz, R. D. Modelling the Effects of Injector Nozzle Geometry on Diesel Sprays. SAE Paper. 1999-01-0912, 1999.

69. Nurick, W.H. Orifice Cavitation and Its Effect on Spray Mixing. Journal of Fluids Engineering. 1976, 98, 681-687.

70. Reitz, R.D., Modeling atomization processes in high-pressure vaporizing sprays, Atomization Spray Technology. 1987, 3, 309-37.

71. Godsave, G. A. E. Studies of the Combustion of Drops in a Fuel Spray: The Burning of Single Drops of Fuel. Fourth Symposium (International) on Combustion, Williams and Wilkins, Baltimore. 1953, 818-830.

72. Spalding, D. B. The Combustion of Liquid Fuels. in: Proc. 4th Symp. (Int.) on Combustion, Williams and Wilkins, Baltimore, MD. 1953, 847-864.

73. Wise, H.; Lorell, J.; Wood, B.J. The Effects of Chemical and Physical Parameters on the Burning Rate of a Liquid Droplet. Fifth Symposium (International) on Combustion, Reinhold, NY. 1955, 132-141.

74. Amsden, A.A.; Orourke, P.J.; Butler, T.D. KIVA-2: A computer program for chemically reactive flows with sprays. Los Alamos National Lab., NM. NASA STI/Recon Technical Report N 04/1989; 89:27975.

75. Kong S.C.; Han, Z.; Reitz, R.D. The Development and Application of a Diesel Ignition and Combustion Model for Multidimensional Engine Simulation. SAE Paper No. 950278.

76. Bergeron, C.A.; Hiroyasu, H. Ignition Characteristic of Liquid Hydrocarbon Fuels and Single Droplets. Canadian Journal of Chemical Energy. 1989, 67, 142-9.

77. Aithal, S.M. Development of a fast, robust equilibrium chemistry solver for analyses of combustion products. Mathematics and Computer Science Division, Argonne National Laboratory.

78. Lee, B.I.; Kesle,r M.G. A Generalized Thermodynamic Correlation Based on Three-Parameter Corresponding States. AIChE Journal. 1975, 21, 510-527.

79. Reid, R.C.; Prausnitz, J.M.; Poling, B.E. The Properties of Gases and Liquids. 4. Auflage, McGraw-Hill, 1988.

80. Branca, C.; Giudicianni, P.; Di Blasi, C. GC/MS characterization of liquids generated from low-temperature pyrolysis of wood. Industrial and Engineering Chemistry Research. 2003, 42, 3190–202.

81. Creager, N. Experimental Study of Bio-oil gasification for Syngas production. Thesis, Iowa State University, Ames, Iowa 2015.